An Integrated Reaction Model of Guaiacol Hydrodeoxygenation Using Activated Carbon Supports: Effects of Support Properties, Metals, and Solvents*

Lei Yu[a,b,1], Robert X. Gottlieb[a,c,1], Jeffrey Page[a,b], Julia A. Valla[a,b,*], Matthew D. Stuber[a,c,*]

[a] *Department of Chemical & Biomolecular Engineering, University of Connecticut, Storrs, 06269, CT, USA*

[b] *Center for Clean Energy Engineering, University of Connecticut, Storrs, 06269 CT, USA*

[c] *Process Systems and Operations Research Laboratory, University of Connecticut, Storrs, 06269, CT, USA*

Abstract

The hydrodeoxygenation (HDO) of guaiacol, a model compound for lignin-derived pyrolysis oils, was investigated using Ru and Ni catalysts supported on activated carbons derived from both commercial and renewable (food waste) sources. Comprehensive characterization of support properties including porosity, surface area, hydrophobicity, and morphology revealed their significant influence on catalyst performance. Liquid-phase HDO reactions were conducted in both aqueous and organic (decane) environments to evaluate solvent effects on reaction pathways and product distributions. Ru-based catalysts demonstrated superior activity compared to Ni-based catalysts, while supports with higher mesoporosity facilitated better metal dispersion and enhanced catalytic performance. Notably, food waste-derived activated carbon supports performed comparably or better than commercial activated

*Author's final accepted version. Published version: Yu, L., Gottlieb, R.X., Page, J.R., Valla, J.A., and Stuber, M.D. An integrated reaction model of guaiacol hydrodeoxygenation using activated carbon supports: effects of support properties, metals, and solvents. 10, (2025) pp 2148–2169. DOI: 10.1039/d5re00179j

*Co-corresponding authors.

Email addresses: ioulia.valla@uconn.edu (Julia A. Valla), stuber@alum.mit.edu (Matthew D. Stuber)

[1] Authors share co-first authorship.

carbon when combined with Ru, indicating their potential as sustainable catalyst supports. Mathematical optimization techniques were employed to estimate kinetic parameters and elucidate reaction pathways, revealing notable differences between aqueous and organic media. Specifically, methoxycyclohexanone dominated in organic medium, while cyclohexanol prevailed in aqueous medium. The optimization study identified that cyclohexanol was not an intermediate for cyclohexane production, contrary to conventional understanding. Diffuse Reflectance Infrared Fourier Transform Spectroscopy (DRIFTS) analysis provided insights into adsorption phenomena, explaining carbon balance discrepancies observed particularly in aqueous-phase reactions. This integrated experimental and computational approach advances the understanding of guaiacol HDO reaction mechanisms and provides guidance for the rational design of efficient catalysts for bio-oil upgrading.

Keywords: reaction mechanisms, kinetic parameter estimation, renewable resources, mathematical programming, optimization

1. Introduction

The extraction of clean and renewable energy from biomass resources has attracted much attention in recent years as a result of increasing energy demands and environmental concerns stemming from the excessive use of fossil fuels.[1,2] One promising alternative to traditional crude oil is bio-oil derived from the pyrolysis of biomass.[3,4] However, the bio-oil obtained from direct pyrolysis consists mainly of oxygenates such as cresols, syringols, and guaiacols, among others.[5] The high oxygen content makes bio-oil unstable, acidic, and of low heating value.[6] Thus, bio-oil needs to be upgraded prior to its use. During the catalytic fast pyrolysis (CFP) of biomass, catalysts are employed to deoxygenate bio-oil,[7,8] but unfortunately CFP removes oxygen in the form of CO or CO_2, which undermines the amount of carbon in the derived upgraded biofuel.[9]

Hydrodeoxygenation (HDO) is an alternative to CFP that can remove oxygen in the bio-oil without loss of carbon, although it requires operation under a high-pressure H_2 atmosphere.[10,11] The HDO of bio-oil can be performed in either the liquid phase[5,12,13] or the gas phase.[14–17] Various catalyst supports have been studied for the HDO of phenolic compounds, including *metal oxides* (CeO_2,[15] ZrO_2,[18] TiO_2,[19,20] and Al_2O_3[10,11,21]), *mesostructured silica* (SBA-15[21,22] and MCM-41[21]), *zeolites* (ZSM-5,[23,24] Y zeolite,[6,12]

and HBeta[25,26]), and *carbon supports* (activated carbon,[27,28] carbon nanotube,[14,29,30] and carbon nanofiber[31,32]). Considering metal oxide catalysts, the conventional Al_2O_3 has a relatively low activity and a high coke yield, and while other metal oxides such as ZrO_2 and TiO_2 perform better, they are more expensive and have lower surface areas than Al_2O_3.[33] Mesoporous silica is recognized as an effective support for HDO reactions due to its uniform channels, large pore size, and high surface area.[34,35] However, it is not stable in hot, pressurized water.[36] Zeolites have been widely used in refineries and show very high activity in HDO reactions; however, their high acidity, which promotes their HDO efficiency, can also lead to rapid deactivation due to the strong adsorption and trapping of phenolic compounds in their frameworks.[37,38] Compared to these supports, carbon supports have shown great advantages due to their low cost, high surface area, high hydrothermal stability, and high resistance in acidic and basic media.[30] Additionally, they can be chemically modified to add functional groups on their surfaces, while their active phase (e.g., metals) can be recovered and recycled by burning away the carbon.[39,40] As another key benefit, carbon supports can be prepared from biomass resources, making the overall HDO process renewable and environmentally friendly.[39]

Several studies have recently been published on the HDO of crude bio-oils. Shafaghat *et al.*[41] reported the HDO of crude pyrolysis bio-oil in supercritical methanol using various Ni catalysts supported on HBeta, Si-HBeta, HZSM-5, HY, and Al-SBA-15. Their results revealed a reduction of the oxygen content and an increase in the heating value of the upgraded bio-oil. Oh *et al.*[42] conducted the HDO of crude bio-oil in a continuous-flow fixed-bed reactor using Ni/C, Ni/SBA-15, Ni/Al-SBA-15, and NiMn/SBA-15 as catalysts. Ethanol was used as a solvent and was co-fed with bio-oil into the reactor. The results also showed a lower oxygen content and an improved higher heating value (HHV) for the upgraded bio-oil.[42] Quantitative analysis demonstrated that sugars, aldehydes, and acids were converted into phenols and ketones after upgrading.[42] However, understanding the reaction pathways and kinetics of upgrading real crude bio-oils is very challenging due to the presence of a large number of chemical species.

A reasonable alternative is to study model compounds, which can help identify and understand individual reactions.[43] Commonly used model compounds include phenol,[44] anisole,[45] guaiacol,[46] cresol,[47] and vanillin,[48] which are all frequently found in crude bio-oil. Of the aforementioned model compounds, guaiacol is particularly interesting because it appears in high concen-

tration in lignin-derived pyrolysis oils and it possesses a variety of functional groups, including C-OAr, C-OMe, and C-OH.[49] Additionally, guaiacol dissolves in both water and organic solvents, meaning that the performance of catalysts can be comprehensively evaluated and the reaction mechanism can be understood under different environments.

Many studies on the HDO of guaiacol have recently been published. Hu *et al.*[50] investigated the HDO of guaiacol in a batch reactor using *n*-hexane as the solvent at initial pressure range of 0.5-3 MPa (at room temperature) and reaction temperature range of 160-240 °C. Three Pd catalysts supported by Mordenite, HZSM-5, and HBeta were used.[50] The results suggested that the type of catalyst support had a significant effect on the product selectivity.[50] In addition to cyclohexane, which was the fully hydrogenated and deoxygenated target product, many other ring-coupling products were detected, such as 1,1-bicyclohexyl and (cyclopentylmethyl)cyclohexane.[50] Jeong *et al.*[51] recently used Re catalysts supported on various oxides (SiO_2, Al_2O_3, TiO_2, CeO_2, ZrO_2) for the HDO of guaiacol. The experiments were carried out in the liquid phase using *n*-heptane as the solvent at initial pressure of 2 MPa (20 bar) and reaction temperature range of 200-280 °C.[51] Of the catalyst-support combinations tested, Re/SiO_2 had the highest activity with guaiacol conversion of 98% and a high selectivity to cyclohexane/benzene.[51] The addition of active metals can play an important role in HDO reactions, with Ru and Ni representing two common choices in literature.[52] Ru has been identified as one of the most promising metals for HDO catalysts.[52–54] Ni, as a transition metal, represents a more inexpensive alternative which has also shown good activity in several studies.[55,56]

The properties of the solvent also play a key role during liquid-phase HDO reactions. First, the acidity of the solvent is important. Zhao *et al.*[57] conducted a series of aqueous-phase HDO reactions of phenol using various catalysts in solutions with different acidity. Their results showed that, in neutral or basic solvent, phenol was mainly converted into cyclohexanol by any of the catalysts used, with no cyclohexane produced.[57] However, in an acidic solvent, cyclohexanol was further converted into cyclohexane, especially when stronger acid was used.[57] They claimed that there might be a synergetic effect between hydronium ions and metals.[57] In addition to the acidity of the solvent, the polarity of the solvent plays an important role in catalyst performance. The research carried out by Ranaware *et al.*[30] investigated vanillin HDO reactions catalyzed by ZnO/Co@N-CNT in five solvents of ranging polarities, from *n*-hexane to water. They found that the conver-

sion of vanillin was boosted when more polar solvents were used. This might be attributed to the increased hydrophilicity of the catalyst from N-doping.[30] With a more hydrophilic catalyst, a hydrophilic solvent could facilitate diffusion of the substrate to the catalyst surface. In a study conducted by Zhang *et al.*[58], Ru supported on Nb_2O_5/C was utilized for the HDO of phenol. Their results showed that the use of a biphasic solvent (decalin and water) could improve the selectivity to benzene. Notably, no cyclohexane was produced when water was present. They concluded that the combination of metal oxide and carbon acted as a hydrophobic-hydrophilic material that could stabilize oil-in-water emulsions which therefore enhanced the production of benzene.[58] Qi *et al.*[59] compared the performance of Ni/AC and Ni/HZSM-5 in water and hexane on the HDO of eugenol. They found that the AC-supported catalyst showed better performance in terms of conversion and selectivity to hydrocarbons in water, while HZSM-5 showed better performance in hexane.[59] According to a study carried out by Barton *et al.*[60], the polar solvent may act to inhibit ring saturation reactions during HDO.

Although activated carbons have been widely used as catalyst supports, the effects of their properties on the HDO reaction are not fully understood. The interaction of AC supports and solvents during HDO reactions is also not yet clear. Therefore, in this work, we combine experimental and computational studies to: 1) understand the effects of metals, AC supports, and solvents on the catalytic performance of the HDO of guaiacol; and 2) propose a reaction mechanism that describes the HDO of guaiacol and estimate its kinetic parameters. To achieve these objectives, various AC supports were obtained using different sources (fossils and renewables), varying their intrinsic properties. The formulated ACs were impregnated by two metals, Ru and Ni, and the HDO reactions of guaiacol were performed in decane and water. The reaction mechanism was then elucidated by employing a mathematical optimization approach to identify the kinetic parameters that best described the experimental data. This approach simultaneously ruled out unlikely pathways in the reaction mechanism and provided estimates of the rate constants for the probable reactions in the mechanism.

2. Methods

2.1. Materials

Three activated carbons were used in this study: commercial activated carbon (CAC) provided by Cabot Corp. (Boston, MA, USA), and food-

waste-derived activated carbon (AC) in microporous and mesoporous forms (FWAC-micro and FWAC-meso). The food waste was obtained from the Dining Services Department at the University of Connecticut (Storrs, CT, USA). Ethyl acetate, octane, decane, and pentanol were purchased from Alfa Aesar Chemicals (Haverhill, MA, USA). Isopropanol was purchased from Fisher Chemical (Waltham, MA, USA). Methoxycyclohexanone was purchased from TCI America (Portland, OR, USA). Guaiacol, cyclohexane, cyclohexanol, cyclohexanone, phenol, nickel nitrate hexahydrate, and ruthenium chloride hydrate were purchased from Sigma-Aldrich (St. Louis, MO, USA). Gases including helium, argon, and hydrogen were purchased from Airgas, Inc. (Radnor, PA, USA).

2.2. Catalyst Preparation

FWAC-micro and FWAC-meso were prepared in the lab via two-step physical activation. The detailed protocol can be found in a previous publication by the authors Yu *et al.*[61]. Briefly, the washed food waste was first pyrolyzed at 525 °C for 2 h, and the resulting biochar was then physically activated via steam. FWAC-micro was activated at 850 °C for 3 h and FWAC-meso was activated at 950 °C for 3 h.

All AC supports were impregnated with 10 wt.% Ni or 5 wt.% Ru using the incipient wetness impregnation method.[6] The impregnation agents ($Ni(NO_3)_2{\cdot}6H_2O$ or $RuCl_3{\cdot}xH_2O$) were first dissolved in DI water with the amount required to saturate the corresponding amount of AC. The prepared solution was then added to the AC dropwise until the entire solution was used. The slurry was then dried at 80 °C in an oven for 12 h. Lastly, the dried materials were calcined at 550 °C for 2 h in Ar and reduced at 550 °C for 4 h in H_2. All of the reduced catalysts were used immediately after they were prepared.

2.3. Catalyst Characterization

N_2 adsorption-desorption was performed to determine the surface area and porosity of the AC supports using a Micromeritics (Norcross, GA, USA) ASAP 2020 Sorption Analyzer. All materials were degassed at 120 °C for 12 h under vacuum prior to measurement. N_2 adsorption-desorption isotherms were collected at 77 K under a liquid nitrogen environment. Surface areas of samples were calculated using the Brunauer–Emmett–Teller (BET) method. The total pore volumes were calculated by the single point method below $P/P_0 = 0.99$, and the micropore volume was derived from the t-plot. The

pore size distribution was determined via the Barrett–Joyner–Halenda (BJH) method.

Elemental analysis and inductively coupled plasma optical emission spectroscopy (ICP-OES) were conducted to determine the elemental composition of the AC supports. Carbon, nitrogen, hydrogen, and sulfur content were measured by elemental analysis using an Elementar (Langenselbold, Hessen, Germany) Vario Microcube analyzer, while other elements (calcium and phosphorous) were measured by a PerkinElmer (Waltham, MA, USA) 7300DV Dual View ICP-OES. X-ray diffraction (XRD) patterns of the AC supports were obtained using a Bruker (Billerica, MA, USA) D8 Advance powder diffractometer (CuKα radiation source). Scanning electron microscopy (SEM) was performed to study the morphology of the AC using an FEI (Hillsboro, OR, USA) Quanta FEG 250 scanning electron microscope operating at a potential of 10 kV. The particle size distributions of the AC supports were measured by a Micromeritics Saturn DigiSizer II analyzer with a liquid sample handling unit. Contact angle measurements were conducted using a ramé-hart (Succasaunna, NJ, USA) Model 100 goniometer.

ICP-OES and H_2 chemisorption were performed to measure the metal loading and metal dispersion, respectively. H_2 chemisorption was performed using a Micromeritics ASAP 2020C Sorption Analyzer equipped with a furnace. Each sample was reduced in situ using pure H_2 at 450 °C for 4 h, then degassed at the same temperature for 12 h under vacuum before measurement. Isotherms were collected at 35 °C with pressures ranging from 0.02 MPa to 0.036 MPa. A linear fit of the irreversible isotherm plot was used to determine the quantity of hydrogen adsorbed to create a monolayer. Based on the quantity of hydrogen adsorbed the dispersion was calculated using a stoichiometric factor of 2 (one H_2 adsorbs onto two metal sites) and the mass of metal used (typically $\sim$0.06 g).

2.4. Liquid-Phase HDO Experiments

The HDO reactions of guaiacol by various catalysts were carried out in a stirred stainless steel autoclave reactor (100 mL, Parr Instruments (Moline, Illinois, USA)) fitted with a gas entrainment impeller. Experiments were performed at 250 °C and a constant pressure of 5.17 MPa (750 psi), with a stirring rate of 900 rpm. HDO reactions were conducted in either the aqueous phase or the organic phase, where either water or decane was used as the solvent, respectively. The quantities of components added to the reactor were different for the aqueous and organic-phase reactions due to the limitations of

the autoclave volume, the solubility of guaiacol in water, and the detection limit of the GC-MS. For aqueous-phase reactions, 55 mL of water and 1 g of guaiacol were initially loaded into the reactor, while for organic-phase reactions, 51.4 mL of decane, 1.6 g of guaiacol, and 1.1 mL of octane were loaded into the reactor. Octane was added as an internal standard for the organic-phase reactions, while pentanol was added as the internal standard for the aqueous-phase reactions. Pentanol was added directly to samples to avoid it being involved in any reactions. The quantity of catalyst used was 0.1 g for all experiments.

Before starting the reactions, the reactor was filled with Ar and a leak test was performed. The reactor was then depressurized and purged with H_2. Next, the reactor was heated to 250 °C (with an average heating rate of 10 °C/min) and the impeller was engaged. Once the target temperature was achieved, the reactor was pressurized to the desired pressure, and the reaction clock started. H_2 was supplied continuously to maintain the reactor pressure during the experiment. Liquid samples were collected from the reactor using a custom-made sampling system. The intervals for sampling were not constant and depended on the overall reaction rates for the different catalysts. The total reaction duration was 120 min, unless the reaction was completed earlier. All experiments were repeated three times to ensure the accuracy of the data.

The liquid samples were processed before performing the analysis. For the organic-phase reactions, the collected samples were diluted to appropriate concentrations using isopropanol and filtered to remove the catalyst. For aqueous-phase reactions, ethyl acetate and the internal standard (pentanol) were added to the samples. The upper layer (ethyl acetate later) of the biphasic liquid mixture was then separated and filtered to remove the catalyst, and then analyzed.

Concentration measurements of the products and reactant were carried out by gas chromatography equipped with mass spectrometer (GC-MS, Agilent (Santa Clara, CA, USA) 6890 GC with 5673 MS), using a previously described method.[12] The GC-MS was calibrated externally for all observed chemical species using the corresponding chemical standards. Calculations of conversion x, selectivity of the i-th product S_i, carbon balance ξ, and yield

of the i-th product Y_i were, respectively, based on the following:

$$x = 1 - \frac{c_g}{c_g^0}, \tag{1}$$

$$S_i = \frac{c_i}{\sum_{j \in \{\text{products}\}} c_j}, \tag{2}$$

$$\xi = \frac{\sum_{j \in \{\text{products}\}} m_j^{\text{c}} + m_g^{\text{c}}}{m_g^{\text{c},0}}, \tag{3}$$

$$Y_i = \frac{c_i}{c_g^0}, \tag{4}$$

where c_g is the molar concentration of guaiacol in liquid phase determined by GC-MS, c_g^0 is the initial molar concentration of guaiacol (at $t = 0$), c_i is the molar concentration of the i-th product, m_g^{c} is the mass concentration of carbon in the guaiacol in the liquid phase, $m_g^{\text{c},0}$ is the initial mass concentration of carbon in the guaiacol (at $t = 0$), and m_j^{c} is the mass concentration of carbon in the j-th product.

2.5. Adsorption Experiments of Guaiacol on Catalysts by DRIFTS

The adsorption of guaiacol on catalysts was studied with diffuse reflectance infrared Fourier transform spectroscopy (DRIFTS) using a Thermo Scientific (Waltham, MA, USA) Nicolet 6700 FTIR with an MCT detector and a temperature-controlled Harrick Scientific (Pleasantville, New York, USA) Praying Mantis DRIFTS assembly. DRIFTs samples were prepared by mixing catalysts with KBr in a 1:9 ratio (catalyst:KBR). The spectra of catalysts themselves were taken at 120 °C under vacuum. In-situ adsorption of guaiacol was then performed at 40 °C with nitrogen flow. It should be noted that N_2 atmosphere was chosen for the DRIFTS studies rather than H_2 to isolate and study only the adsorption of guaiacol on the catalytic surface, rather than any reactions. After adsorption, the system was pulled under vacuum and the cell was heated at a heating rate of 10 °C/min until the characteristic peaks of guaiacol disappeared. The spectra were taken every 40 °C. The catalysts during and after HDO reactions were also extracted for DRIFTS analysis to compare the adsorption phenomena of guaiacol under reaction conditions and atmospheric conditions. The spectrum of guaiacol was also collected as a reference.

2.6. Kinetic Modeling of HDO Reactions

To investigate the catalyst- and solvent-dependent reaction pathways of guaiacol HDO, kinetic models were created for comparison with experimental data. Similar to the predictive modeling approach described by Green[62], the HDO mechanism is broken down into individual reaction steps that are likely to occur on the catalyst surface, which are then combined to form a "complete" model. Conceptually, this approach is also similar to the dynamic flux balance analysis (DFBA) method used in computational biology. In DFBA, systems are macroscopically represented by creating transient mass conservation equations with first-order conversion and consumption rates for each reacting species.[63] The representation is created by multiplying a matrix of reaction stoichiometries by rates of change for each species, which results in a linear system.[63] Despite the complexity and nonlinearity of underlying biological reaction mechanisms, this flux balance approach has found success in a variety of applications that rely on elucidating metabolic pathway utilization.[64]

We employ a similar method here to study the catalytic reaction pathways of the HDO reactions. The goal of this approach is to obtain effective rate coefficients based on mass balances, which will highlight the relative importance of each potential reaction path. By including every possible path in our complete model, this generates information on which paths are most likely to occur. It is also important to highlight that the effective rates that appear in this model are inherently macroscopic in nature, and are not intended to provide specific details about the reaction mechanism as it occurs on the catalyst surface. The evolution of each chemical species in this complete model is described as:

$$\begin{aligned} \frac{d}{dt}\mathbf{c}(\mathbf{p},t) &= \boldsymbol{\omega}(\mathbf{c}(\mathbf{p},t)),\ t \in I = [0, t_{\text{end}}], \\ \omega_i(\mathbf{c}(\mathbf{p},t)) &= \sum_{j=1}^{n_r} \nu_{ij} r_j(c_j(\mathbf{p},t), p_j),\ i = 1, \ldots, n_s, \\ \mathbf{c}(\mathbf{p},0) &= \mathbf{c}_0, \end{aligned} \tag{5}$$

where n_s and n_r represent the number of species and reactions in the model, respectively; $\mathbf{c} : P \times I \to \mathbb{R}^{n_s}$ represents the concentrations of species as the parametric solution of the ordinary differential equation (ODE) system (5) with the initial conditions given as $\mathbf{c}_0 \in \mathbb{R}^{n_s}$; $\boldsymbol{\omega} : \mathbb{R}^{n_s} \to \mathbb{R}^{n_s}$ is the vector of instantaneous rates of change of the n_s species (i.e., the right-hand-side

function of the ODE); $\nu_{ij} \in \mathbb{Z}$ is the stoichiometry of the i-th species in the j-th reaction; $r_j : \mathbb{R} \times P_j \to \mathbb{R}$ is the rate of the j-th reaction, defined later in (6); and $\mathbf{p} \in P \subset \mathbb{R}^{n_p}$ is the vector of *unknown* model parameters comprised of the effective rate constants as $\mathbf{p} = (k_{\text{eff},1},\ k_{\text{eff},2},\ \ldots,\ k_{\text{eff},n_p})$, to be estimated with mathematical optimization.

Experimentally, concentrations are measured in the bulk solvent, but the reactions themselves occur on the catalyst surface after adsorption. Various techniques such as surface-enhanced Raman spectroscopy[65] have been used to measure the concentrations of transient reaction intermediates on catalytic surfaces, but such techniques do not apply to this experiment as the catalyst is dispersed throughout the bulk phase. This inability to measure species concentrations on the catalyst presents a challenge for model development, as the concentrations of reacting species are unknown at all time points. Consequently, several considerations were made in the construction of the overall model:

1. It was assumed that the bulk concentrations of chemical species remained roughly proportional to the concentrations of adsorbed species throughout the experiment. In addition to the assumption that each reaction is irreversible, this allowed us to model each reaction rate as:

$$r_j = k_{\text{eff},j} c_j. \tag{6}$$

2. Analogous to DFBA, (6) represents first-order generation and consumption of individual species j, and does not itself imply that reactions on the catalyst are first-order in nature. Consequently, k_{eff} does not represent the rate constant of any fundamental mechanism but is instead related to the reaction pathways macroscopically.
3. Due to the possibility of adsorption/desorption of species onto/from the catalyst surface, any measurement of species concentrations during the experiment may appear to violate mass continuity. To account for this, a "placeholder species" was included in the model (i.e., a *slack* variable) that balances the total concentration so that it remains constant.
   DRIFTS measurements of used catalysts described in Section 3.5 indicated that guaiacol was the dominant non-desorbed species on the catalyst surface. And so, for the simplicity of the model, it is assumed that only guaiacol contributes to the material balance deviation. That is, only guaiacol can add to the placeholder species, and if the total species balance requires flux from the placeholder species, it is assumed that

the molecules desorb as guaiacol. Without this assumption, if we assumed that adsorption and desorption could arise from any species, the model would require an additional $2n_s - 2$ parameters; the addition of which could make the parameter estimation problem significantly more computationally expensive as well as introduce issues of overfitting.

4. It is possible that a molecule will adsorb onto the catalyst and undergo multiple reaction steps before finally desorbing. Therefore, when creating the complete model, reactions were included that connect each chemical species to every product that might arise further down the proposed reaction pathway. The purpose of creating such a combinatorial reaction network is not to suggest that every possible forward reaction is occurring, but rather to rely on parameter estimation with mathematical optimization to determine which reactions are unlikely to be occurring based on experimental observation, and thus to determine a plausible reaction pathway.

With the j reactions defined as a dynamic ODE system as in (5), for each catalyst tested, we find the parameters that minimize the distance between the experimental data and model predictions in a manner similar to Singer *et al.*[66]. The objective function is defined as:

$$f(\mathbf{p}) = \sum_{k=1}^{n_d} ||\mathbf{d}_k - \mathbf{c}(\mathbf{p}, t_k)||_2^2, \tag{7}$$

which is minimized with respect to $\mathbf{p}$. Here, $\mathbf{d}_k \in \mathbb{R}^{n_s}$ is a vector of experimental concentration data at the k-th time step $t_k \in I$, averaged over all replicate measurements. n_d refers to the number of time points sampled during each experiment.

The resampled inheritance search (RIS) method[67] from the software package `BlackBoxOptim.jl` (v0.6.1)[68] is used to optimize (7). RIS is a stochastic global optimization method: it randomly samples parameter values without the need for any initial guesses and then performs a deterministic local search to locate nearby optimal values. Unlike deterministic global optimization methods such as branch-and-bound,[69–72] RIS does not guarantee that globally optimal solutions are found. However, because of the stochastic sampling, RIS is more capable than methods such as conventional gradient descent at escaping from local minima in the parameter space. For each of the catalysts tested, the RIS algorithm is run for one hour on a single thread of an Intel Xeon E3-1285 v6 4.10/4.50 GHz (base/turbo) processor with 32GB

ECC RAM, running Windows 10, version 21H1, and Julia v1.6.1,[73] to allow the algorithm time to find a reasonable solution. All parameters are searched in the range $k_{\text{eff},j} \in [0.0, 1.0]$ min^{-1}. Within the context of these experiments, a rate of 1.0 min^{-1} is effectively instantaneous, and allowing higher values was found to yield only marginal improvements in the model fit at the expense of a significantly larger search space, due to the high dimensionality of the models.

After optimization, the rate constants that result in the lowest identified error between the model and experiments can be used to provide information about the reaction pathway. Specifically, the species fluxes modeled using the effective rate constants will parallel the reactions occurring on the catalyst surface, and thus high effective rate constants can be interpreted as high catalytic reaction rates for those reaction steps. Similarly, low or near-zero effective rate constants—those below 10^{-6} min^{-1}—are indicative of slow or non-occurring reaction steps on the catalyst. With a full set of effective rate parameters, we can examine the "complete" reaction mechanism and determine which steps are plausible and which are unlikely to be occurring experimentally.

Although the rate constants obtained through this analysis are intended only for qualitative interpretation, it is still important to consider the model's sensitivity to the values of individual kinetic parameters. If the model is very sensitive to a particular rate constant, for instance, that provides evidence that the value of the rate constant was more precisely identified by the optimization, as a small change in its value would substantially affect the model fit. Understanding the variance of the rate constants is also critical when considering that the optimization process is stochastic: rate constants may not be identical if the analysis is repeated multiple times, but with the sensitivities, we can confidently posit how likely the value is to stay the same on different runs. For these reasons, a sensitivity analysis was performed over the parameter space within a neighborhood of the values determined by optimization. First, the points are selected following a Sobol sequence[74] using the `Sobol.jl` (v.1.4.0) package[75] in the region defined by the intersection between the originally searched parameter space and a hypercube of side length 2.0×10^{-5} min^{-1} centered on the optimal solution. Then, the magnitude of the sensitivity of the model to each parameter is calculated as:

$$\left|\frac{\delta f(\mathbf{p}^*)}{\delta p_i}\right| = \frac{1}{n_{\text{Sobol}}} \sum_{j=1}^{n_{\text{Sobol}}} \left|\frac{f(\mathbf{p}_j + \mathbf{e}_i\epsilon) - f(\mathbf{p}_j - \mathbf{e}_i\epsilon)}{2\epsilon}\right|, \; i = 1, \ldots, n_p, \tag{8}$$

where $\mathbf{p}^* \in P \subset \mathbb{R}^{n_p}$ is the optimal solution value, n_{Sobol} is the number of Sobol points used, which is 10^4 in this case, $\mathbf{p}_j \in P \subset \mathbb{R}^{n_p}$ is the parameter vector associated with the j-th point in the Sobol sequence, $\mathbf{e}_i$ is a unit vector in the i-th direction, and ϵ is an arbitrarily small constant, chosen here to be 10^{-7} min^{-1}.

3. Results and Discussion

3.1. Characterization Results

The three AC supports (i.e., CAC, FWAC-meso, and FWAC-micro) were first characterized by measuring their surface areas and pore volumes. The results of this analysis are presented in Table 1. Comparing the surface areas, the CAC support was the highest at 918 m^2/g, and although FWAC-meso had a lower micropore volume than FWAC-micro, it had a higher surface area due to its higher mesopore volume. The presence of mesoporosity in CAC and FWAC-meso was confirmed by their N_2 sorption-desorption isotherms, shown in Figure 1, which show typical Type IV isotherm curves. On the other hand, FWAC-micro showed an isotherm curve closer to Type I, indicating microporosity. Finally, although CAC and FWAC-meso showed similar micropore and mesopore volumes, according to the pore size distributions shown in Figure 2, the average mesopore size of CAC was smaller than that of FWAC-meso, resulting in a higher BET surface area.

Table 1: BET surface areas and pore volumes of the three AC supports. CAC has the highest surface area due to its smaller average mesopore size than FWAC-meso, and FWAC-meso has a higher surface area than FWAC-micro due to its higher mesopore volume. FWAC-micro has the highest micropore volume and the lowest total pore volume.

Sample	BET Surface Area [m^2/g]	t-Plot Micropore Volume [cm^3/g]	Total Pore Volume [cm^3/g]
CAC	918	0.157	0.770
FWAC-micro	622	0.196	0.407
FWAC-meso	684	0.146	0.704

The elemental compositions of the AC supports were determined by an elemental analyzer and ICP-OES. The results are displayed in Table 2. The CAC support showed a carbon content of 64.2%, which was similar to that of FWAC-micro. FWAC-meso contained a carbon content of only 40.9% as a result of the severe burn-off of carbon during the activation process, since

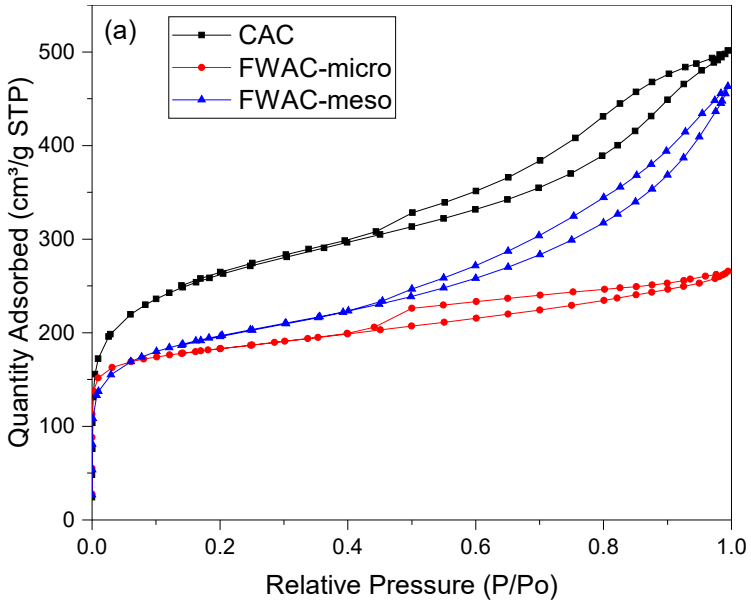

Figure 1: N_2 sorption-desorption isotherms for the three AC supports. CAC and FWAC-meso show typical Type IV isotherm curves, indicating mesoporosity, and FWAC-micro shows an isotherm curve closer to Type I, indicating microporosity.

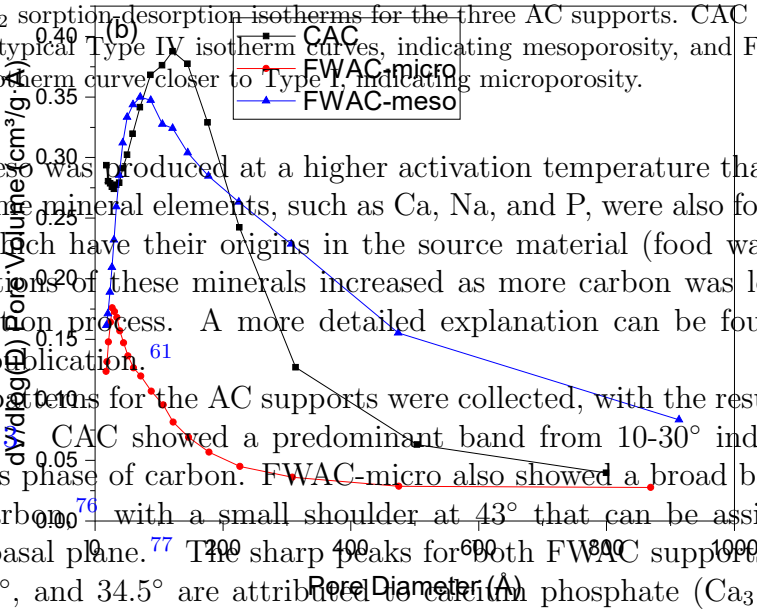

FWAC-meso was produced at a higher activation temperature than FWAC-micro. Some mineral elements, such as Ca, Na, and P, were also found in the FWAC, which have their origins in the source material (food waste). The concentrations of these minerals increased as more carbon was lost during the activation process. A more detailed explanation can be found in our previous publication.[61]

XRD patterns for the AC supports were collected, with the results shown in Figure 2. CAC showed a predominant band from 10-30° indicating an amorphous phase of carbon. FWAC-micro also showed a broad band at 20-30° for carbon[76] with a small shoulder at 43° that can be assigned to a graphite basal plane.[77] The sharp peaks for both FWAC supports observed at 28°, 31°, and 34.5° are attributed to calcium phosphate ($Ca_3(PO_4)_2$).[78] The existence of calcium phosphate in FWAC was also confirmed by the ICP-OES results in Table 2. The characteristic peaks of carbon did not appear in the pattern of FWAC-meso, likely because the carbon content was relatively low.

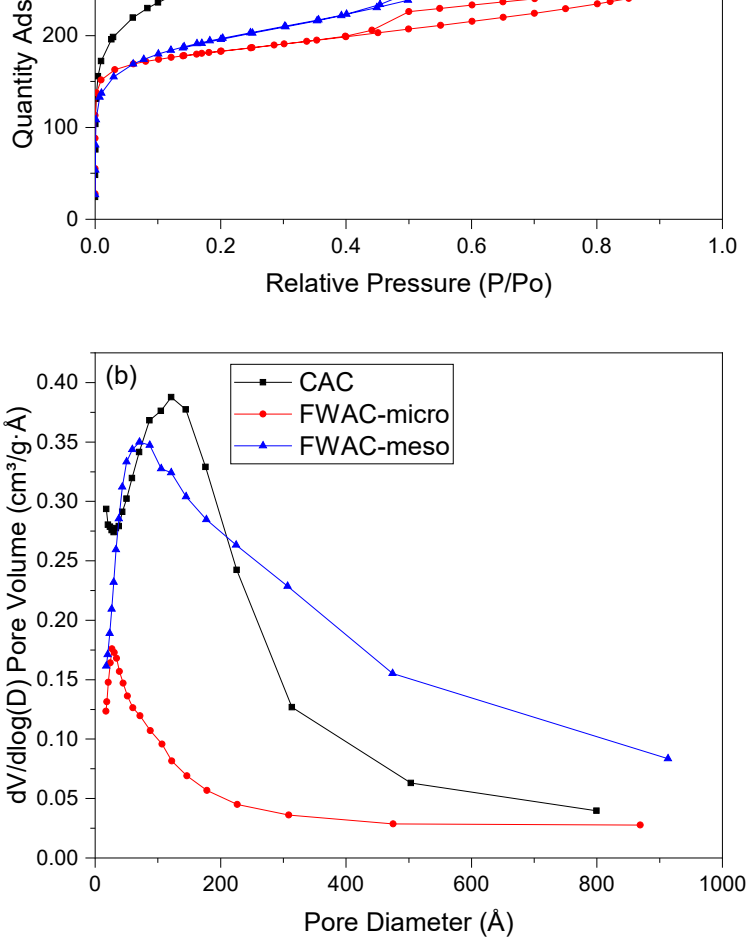

Figure 2: Pore size distributions of the three AC supports. Although CAC and FWAC-meso had similar micropore and mesopore volumes, the average mesopore size of CAC is smaller than that of FWAC-meso. FWAC-micro predominantly has much smaller pores than both CAC and FWAC-meso.

SEM images of the AC supports are presented in Figure 4. The images at low magnification on the far left indicate that the CAC support has a smaller and more homogeneous particle size than the FWAC supports. According to the results of the particle size distribution presented in Supplementary Information Figure S1, the CAC support mainly comprises particles smaller than 100 μm, whereas the FWAC supports have a broad distribution of sizes up to 350 μm with an average particle size of approximately 180 μm. Some of FWAC-micro particles exhibited large pieces and protrusions on their surfaces, while the FWAC-meso particles had more pores on their surfaces. Some fibers were also found in the FWAC samples. Under high magnification, the morphologies of CAC and FWAC-meso particles were similar.

The contact angle was measured in triplicate to assess the hydrophobicity of AC, with the results displayed in Table 3. A larger contact angle indicates higher hydrophobicity. These results showed that the CAC support was more hydrophilic than the FWAC supports, and FWAC-micro was slightly more hydrophilic than FWAC-meso. A wettability test was also performed in a

Table 2: Elemental composition of the three AC supports as measured by an elemental analyzer and ICP-OES. FWAC-meso has a notably lower carbon content than the other two supports due to carbon burn-off from its higher activation temperature. Both FWAC supports show elevated concentrations of Ca, Na, and P relative to CAC due to the food waste feedstock used to create them.

Sample	Elemental composition (wt.%)							
	By elemental analysis					By ICP-OES		
	N	C	H	S	Others (by difference)	Ca	Na	P
CAC	1.6	64.2	2.7	0.2	31.3	0.2	-	2.6
FWAC-micro	2.5	62.6	0.5	0.3	34.1	6.5	0.2	3.3
FWAC-meso	1.6	40.9	1.6	0.2	55.7	13.6	0.3	7.8

biphasic water–ethyl acetate system, with the results shown in Supplementary Information Figure S2. FWAC-meso and FWAC-micro particles were dispersed at the interface of water and ethyl acetate, but a number of CAC particles were able to enter and suspend in the water phase. The CAC particles that were stabilized in the ethyl acetate phase were pushed to the wall instead of suspending in the liquid. These observations indicated that CAC was more hydrophilic than FWAC, which is consistent with the results from the contact angle measurements.

Table 3: Contact angle measurements are shown for the three AC supports. Higher contact angles, such as for FWAC-meso, indicate higher hydrophobicity. CAC has the lowest contact angle and is therefore more hydrophilic than both of the FWAC supports.

Sample	Contact Angle			
	#1	#2	#3	Average
CAC	45°	43°	48°	45.3°
FWAC-micro	64°	66°	69°	66.3°
FWAC-meso	69°	65°	73°	69.0°

Table 4 shows the theoretical percentage of metal loading and the actual percentage of metal measured by ICP-OES, as well as the corresponding metal dispersion measured by H_2 chemisorption. In contrast to Ni-FWAC-meso, Ni-CAC and Ni-FWAC-micro showed higher Ni loading than the theoretical value. The lower Ni loading for Ni-FWAC-meso might be attributed to the desorption of functional groups during the calcination process. The Ru-FWAC-micro and Ru-FWAC-meso catalysts showed lower actual Ru loading

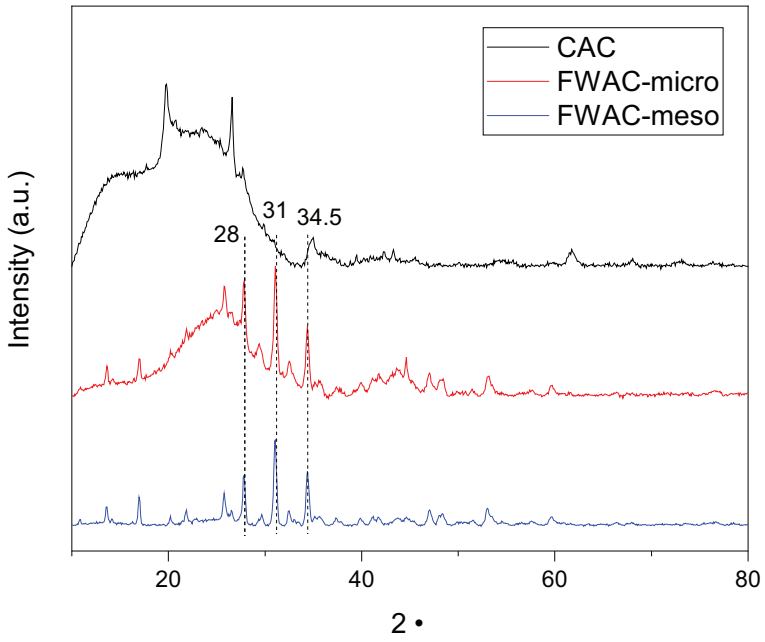

Figure 3: XRD patterns collected for the three AC supports. Sharp peaks at 28°, 31°, and 34.5° that appear in the food waste-derived ACs are highlighted, which are attributed to calcium phosphate.

than the theoretical values. This might be attributed to the hydrophobic nature of FWAC, which caused: 1) the precursor solution to be adsorbed nonuniformly on the support; and 2) the slow penetration of the aqueous metal salt solution into the relatively smaller pores of the hydrophobic carbon support.[79] The dispersion of Ni was very low compared to that of Ru, likely due to the high Ni loading. The dispersion of Ru showed a positive correlation with the mesoporosity of the supports, indicating the importance of mesoporosity for high metal dispersion.[80]

3.2. HDO of Guaiacol in Decane

The HDO experiments of guaiacol were first performed in the organic solvent decane. Each of the prepared catalysts was tested for activity. Figure 8 in Section 3.6 shows the concentrations of the reactant and products during the HDO reactions in decane, along with model fitting results; experiments that did not show any conversion are not displayed. For the Ni-impregnated catalysts, only Ni-FWAC-meso showed activity in decane; no product was

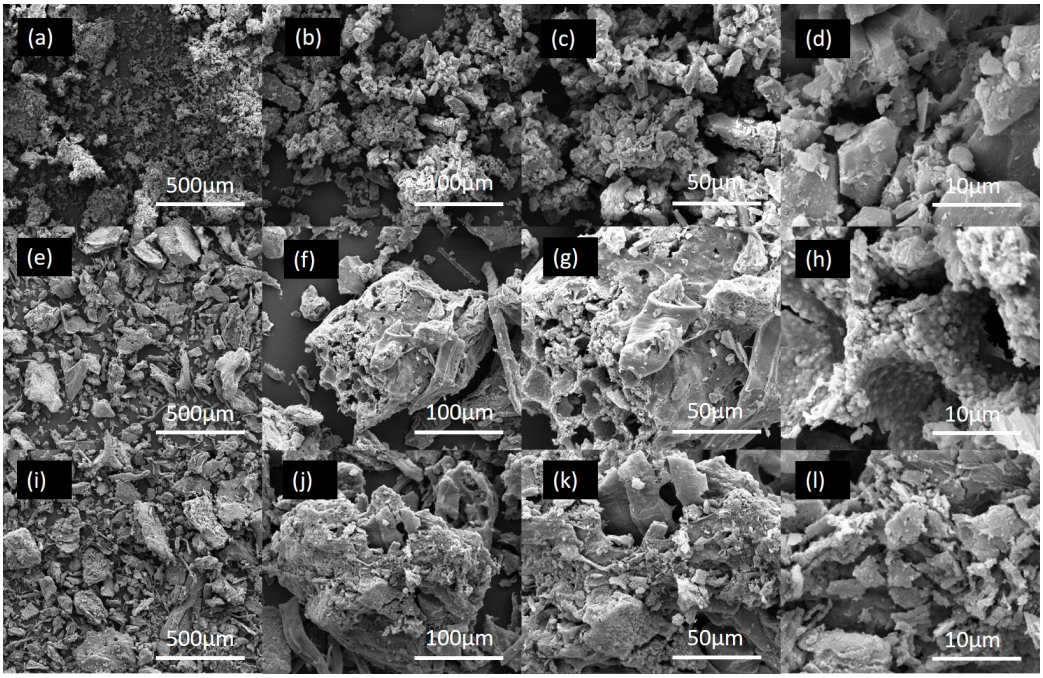

Figure 4: SEM images of the AC supports taken at increasing levels of magnification. The ACs presented are: (a)-(d) CAC, (e)-(h) FWAC micro, and (i)-(l) FWAC meso. CAC shows a smaller and more homogeneous particle size than the FWAC supports, which have broad distributions of particle sizes and some fibers.

detected in liquid samples taken from the Ni-CAC or Ni-FWAC-micro experiments. This could be attributed to differences in the physical properties of the carbon supports. As discussed in Section 3.1, although CAC and FWAC-meso showed similar porosities, and CAC showed a higher surface area than FWAC-meso, CAC was not as hydrophobic as FWAC-meso, which could result in limited interaction between Ni-CAC and the reactant in the solution. Wang *et al.*[81] tested carbon-coated CoS_2-MoS_2 catalysts for the HDO of ethylphenol in dodecane, and they observed that increasing the hydrophobicity of the catalyst can improve its performance. One possible explanation for the improvement was that the higher hydrophobicity could force the water produced during the HDO reaction to leave the active sites of the catalyst and allow the reaction to proceed further.[81] It is worth noting that the higher hydrophobicity also enhanced the dispersion of catalysts in the organic solutions.[81] Therefore, AC supports with higher hydrophobicity might be beneficial to the HDO activity of the catalyst in organic solvent.

Table 4: Theoretical and actual metal loadings for all tested catalysts, as measured by ICP-OES, Ni shows higher loading than its theoretical value for CAC and FWAC-micro, likely due to the desorption of functional groups during the calcination process. Ru shows lower loading than its theoretical value for both of the FWAC supports, likely due to their higher hydrophilicity. Metal surface density based on surface area and actual metal loadings from ICP. Metal dispersion values from H_2 chemisorption are also presented. Ru dispersion is higher for the more mesoporous supports, and Ni dispersion is low for the CAC support, likely due to the high actual Ni loading.

Sample	Metal loading	Actual metal loading by ICP	Metal surface density [atoms/nm^2]	Metal dispersion
CAC	10% Ni	13.0%	1.45	0.27%
	5% Ru	5.1%	0.33	6.80%
FWAC-micro	10% Ni	12.4%	2.05	1.14%
	5% Ru	3.7%	0.35	2.61%
FWAC-meso	10% Ni	9.3%	1.39	1.87%
	5% Ru	4.2%	0.36	6.29%

Although FWAC-micro had a similar hydrophobicity to FWAC-meso, the Ni-FWAC-micro catalyst did not show any activity for guaiacol HDO while the Ni-FWAC-meso catalyst did. This result might be attributed to the low mesoporosity of FWAC-micro, which caused low metal dispersion during the preparation process.[40] With these differences in hydrophobicity and porosity in mind, although Ni-FWAC-meso did present a small amount of HDO activity, the reaction rate was very low and the final conversion after 120 min of reaction was only 50%. Three products from this reaction were observed: methoxycyclohexanone, cyclohexanone, and cyclohexanol, with methoxycyclohexanone and cyclohexanol being the major products. Methoxycyclohexanone is the hydrogenated product of guaiacol, while cyclohexanone and cyclohexanol are products with one O-atom removal from guaiacol. That is, the HDO of guaiacol using Ni-FWAC-meso in decane did not generate any 2O removal products.

All Ru-based AC catalysts showed activity with reaction rates much higher than those of Ni-FWAC-meso. Ru-CAC reached 85% conversion after 120 min of reaction, and cyclohexane started to appear as the desired 2O removal product. For the Ru-based catalysts, methoxycyclohexane (1O removal product) also appeared at very low concentrations. As with the Ni-FWAC-meso reaction, methoxycyclohexanone and cyclohexanol were still the dominant products, and the selectivity was highest for methoxycyclohexanone. Cyclohexanone showed higher concentration at the beginning of the

reaction and later dropped to almost zero for each of the Ru catalysts, suggesting that cyclohexanone could be an intermediate product. The reaction was faster with Ru-FWAC-micro and Ru-FWAC-meso than with Ru-CAC and reached 100% conversion within 40 min and 20 min of reaction time, respectively. The identities of the product species for Ru-FWAC-micro and Ru-FWAC-meso were the same as those of Ru-CAC. However, the final concentration of cyclohexane was significantly lower for Ru-FWAC-micro than for Ru-CAC or Ru-FWAC-meso. This result may be due to differences in the porosity between Ru-FWAC-micro and Ru-FWAC-meso.

To summarize, Ru showed much higher activity than Ni for the reactions in decane. CAC and FWAC-micro only showed catalytic activity when Ru was incorporated as the active phase, and Ru-FWAC-meso was the best catalyst for guaiacol HDO in decane among all catalysts tested in terms of reaction rate and O-removal efficiency.

3.3. HDO of Guaiacol in Water

As discussed in Section 1, the solvent plays an important role during HDO reactions. Hence, to investigate the effects of solvent on HDO performance using AC-supported catalysts, we also performed the reactions using water as the solvent. The evolution of chemical concentrations during HDO reactions performed in water, along with the results of model fitting, are shown in Figure 9 in Section 3.6. For the Ni-impregnated catalysts, the performance was notably different when water was used as the solvent in place of decane. In particular, in the aqueous-phase reaction, only Ni-CAC showed any reactivity (as opposed to Ni-FWAC-meso in decane), which might be attributed to the lower hydrophobicity of CAC compared to that of FWAC-micro and FWAC-meso. This lower hydrophobicity might have allowed for better dispersion of the catalyst in water and thus more overall guaiacol adsorbance. However, as with the Ni-FWAC-meso catalyst in decane, the conversion of guaiacol by Ni-CAC in water remained low, reaching approximately 60% after 120 min.

Interestingly, in the water-solvated reactions, phenol started to appear as an intermediate product that was not present in the decane-solvated reactions, and cyclohexanol rather than methoxycyclohexanone became the dominant product. This change might be related to the polarity of the products: cyclohexanol and phenol are more polar than methoxycyclohexanone. Thus, in the aqueous-phase reactions, they can more easily desorb from the catalysts and dissolve in water, allowing the reaction to proceed along that pathway. Another possible explanation might be that the orientations of

reactants adsorbed on the catalyst surface are affected by the polarity of solvent. Wan *et al.*[82] investigated the HDO of *p*-cresol using Pt/C in water and *n*-heptane. They proposed that in water, the *p*-cresol was adsorbed on the catalyst with a vertical orientation where the hydroxyl group was bound on the catalyst thereby favoring the dehydration reaction.[82] In contrast, in non-polar *n*-heptane, the coplanar adsorption position might be favored, which facilitates the hydrogenation reaction.[82]

Water may also participate in HDO reactions through the stabilization and promotion of different reaction intermediates.[83–85] Shangguan *et al.*[84] investigated the HDO of guaiacol using isotopically labeled guaiacol and DFT simulations finding that water not only enables proton-assisted cleavage of guaiacol's methoxy group but stabilizes its transition state resulting in a decrease in free energy barrier of 22 kJ mol^{-1}. Additionally, no promotional effect was found on ring hydrogenation, suggesting that the change in selectivity compared to non-protic solvents is due to water's participation in the methoxy group cleavage.[84] A similar mechanism might be applied to guaiacol in this work, where water as the solvent might favor the deoxygenation reaction and decane as the solvent might favor the hydrogenation reaction.

Reactions in water occurred much faster on Ru-impregnated supports than on Ni-impregnated supports, but in all cases no 2O removal products, such as cyclohexane, were detected in the product pool. The trends of product concentrations over time were very similar for all three Ru catalysts. For each of these reactions, cyclohexanol was the only major product at the end of reaction, though a notable amount of phenol was present toward the beginning of the reaction. The phenol concentration dropped rapidly, likely because the phenol was hydrogenated and converted to cyclohexanone and cyclohexanol. Cyclohexane and methoxycyclohexane appeared in the decane-solvated reactions but not in the aqueous-phase reactions, which might be attributed to their low solubility in water. Even if they were formed on the active sites of catalysts, their desorption could be inhibited, blocking the catalyst active sites. Therefore, species like cyclohexane and methoxycyclohexane were not favorable in the aqueous-phase reactions.

Overall, although CAC was more hydrophilic than FWAC-micro and FWAC-meso, which could be advantageous in the aqueous-phase reaction, the performance of Ru-CAC was not as good as that of Ru-FWAC-micro or Ru-FWAC-meso. Ru-CAC reached 100% conversion in 60 min, while Ru-FWAC-micro and Ru-FWAC-meso completed the reaction in 30 and 20 min, respectively. The high activity of Ru-FWAC (micro and meso) suggests that

AC produced from renewable resources, such as food waste, can be a great catalyst support for HDO reactions.

3.4. Comparison of HDO Performance in Organic Solvent and Water

Figure 5 summarizes the high-level differences between the decane- and water-solvated reactions by showing the overall conversions and final product selectivities. Panels (a) and (b) show that in each solvent, the reaction rates and guaiacol conversion are higher for every Ru-based catalyst than for any Ni-based catalyst. For the Ni catalysts specifically, only Ni-FWAC-meso for decane and Ni-CAC for water showed any activity. As discussed previously, the FWAC-meso and CAC supports had very similar porosities and microstructures, but Table 3 indicates that CAC is more hydrophilic than FWAC-meso. The hydrophilicity of CAC allowed better contact and adsorption of the guaiacol molecules in water, resulting in the better performance of Ni-CAC, and similarly, the hydrophobicity of FWAC-meso led to the better performance of Ni-FWAC-meso in decane. Another possible explanation for this observed difference in performance is that the Ni-CAC has a lower dispersion (0.27%) compared to the Ni-FWAC-meso (1.87%) which would result in fewer accessible active sites and potentially different electronic properties of the Ni sites.

Panels (c) and (d) of Figure 5 show the final selectivities of the products in each reaction. Most notably, methoxycyclohexanone and cyclohexanol are the major products in both solvents, but methoxycyclohexanone is favored in decane and cyclohexanol is strongly favored in water. Additionally, cyclohexane is present as a product in decane-solvated reactions with Ru-based catalysts but does not appear in any of the water reactions. Similarly, phenol is not present in any of the decane-solvated reactions, but it is present as an intermediate species in every water-solvated reaction and as a final product in the slow Ni-CAC-catalyzed reaction. These differences might be attributed to the relative polarity and solubility of the products. Decane is a nonpolar solvent, cyclohexane is a nonpolar molecule, and methoxycyclohexanone is less polar than cyclohexanol. The presence of decane as the solvent thus allowed these species to desorb from the catalyst surface more readily. The absence of cyclohexane in the aqueous-phase reaction was also observed by Zhang *et al.*[58]. It is likely that water as the solvent hinders the formation of nonpolar chemicals during HDO reactions. When the nonpolar species are formed on the catalyst surface, they cannot be desorbed to the surrounding aqueous phase, and their further formation is inhibited.

Additional final product yield and carbon balance data for both the water- and decane-solvated experiments can be found in Supplementary Information Table S1.

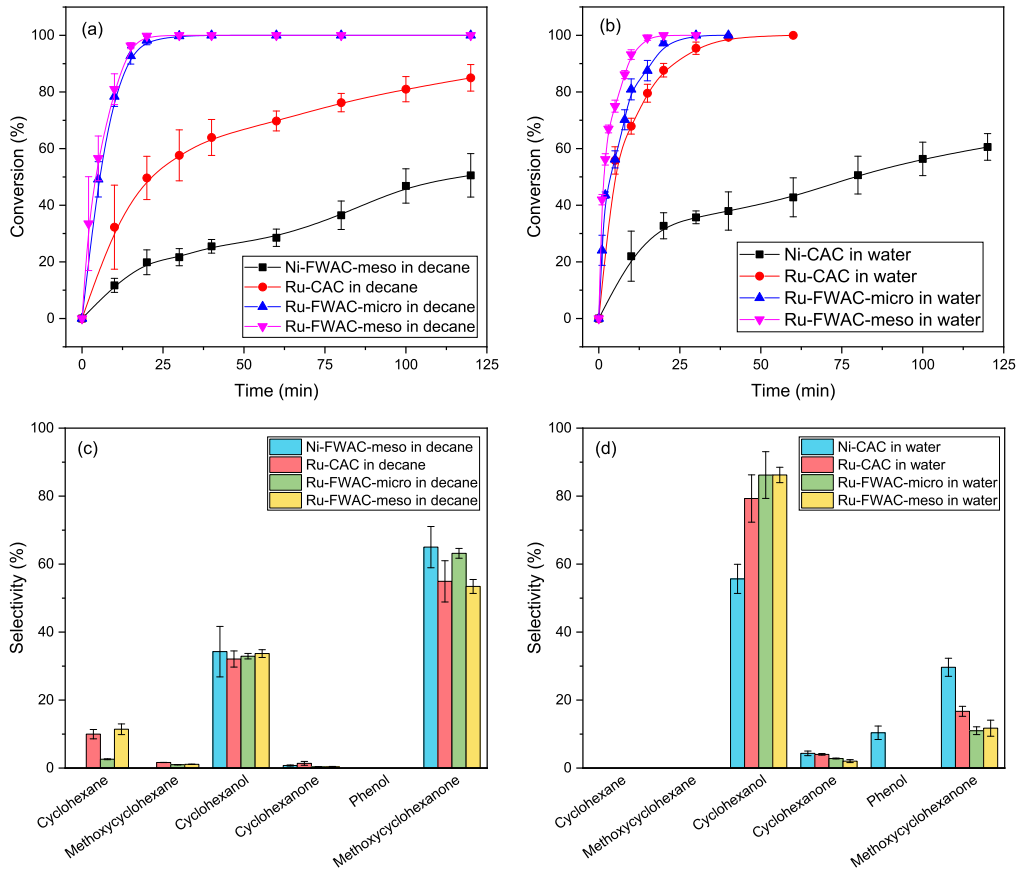

Figure 5: Guaiacol HDO conversion is presented as a function of time for reactions in (a) decane and (b) water. In both decane and water, the Ru-FWAC catalysts showed faster conversion than the Ru-CAC catalyst. For Ni, only Ni-FWAC-meso showed activity in decane, and only Ni-CAC showed activity in water. This is likely related to the hydrophobicity of the supports. The final product selectivities for each catalyst are also presented for the reactions in (c) decane and (d) water. Methoxycyclohexanone is the dominant product for the decane-solvated reactions, and cyclohexanol is more highly dominant in the water-solvated reactions. This difference is attributed to the product polarities in relation to the solvent polarity.

Sample	Metal loading	Organic phase	Aqueous phase
CAC	10% Ni	0%	60.6%
	5% Ru	85.0%	100%
FWAC-micro	10% Ni	0%	0%
	5% Ru	100%	100%
FWAC-meso	10% Ni	50.6%	0%
	5% Ru	100%	100%

Table 5: The guaiacol HDO final conversions in reactions with each catalyst are summarized. Each of the Ru-based catalysts showed 100% conversion in both solvents, with the exception of Ru-CAC in decane. Only two of the six Ni-catalyzed reactions showed any activity and their conversion remained below 100% after 120 minutes of reaction.

3.5. Adsorption Study of Guaiacol on Catalysts

In previous sections, we discussed the experimental results of guaiacol HDO under different catalyst and solvent conditions. During the experiments, it was observed that the carbon balance of the reactions conducted in the aqueous phase was low (Supplementary Information Table S1), whereas such an issue did not appear in the organic-phase reactions. To understand the origin of the low mass balance in the aqueous-phase experiments, we performed in-situ adsorption studies of guaiacol on the Ni-CAC and Ru-CAC catalysts in a DRIFTS cell. Guaiacol was first flowed through the cell carried by N_2 until the catalyst was saturated. The cell was then pulled under a vacuum to remove physisorbed guaiacol, followed by temperature-programmed desorption. The adsorption results of Ni-CAC and Ru-CAC are shown in Figure 6 panels (a) and (b), respectively. Breaks were added to the spectra to clarify the characteristic peaks of guaiacol. For Ni-CAC, several strong adsorption peaks were observed at 1500, 1257, and 742 cm^{-1}, which corresponded to the aromatic ring vibration, the C-O vibration of the phenolic group, and the C-H vibration of ortho-disubstituted benzene, respectively.[86–88] Other weak peaks between 1223 and 1024 cm^{-1} were attributed to the C-O aromatic ether bond and C-O stretching of the methoxy group.[88] The peaks located at 836, 789, and 700 cm^{-1} were attributed to C-H bonds on aromatic rings. No other bands were found at higher wavenumbers. As the temperature increased, the characteristic peaks of guaiacol gradually disappeared, indicating that guaiacol was being desorbed from the catalyst. The desorption process was completed at approximately 240 °C.

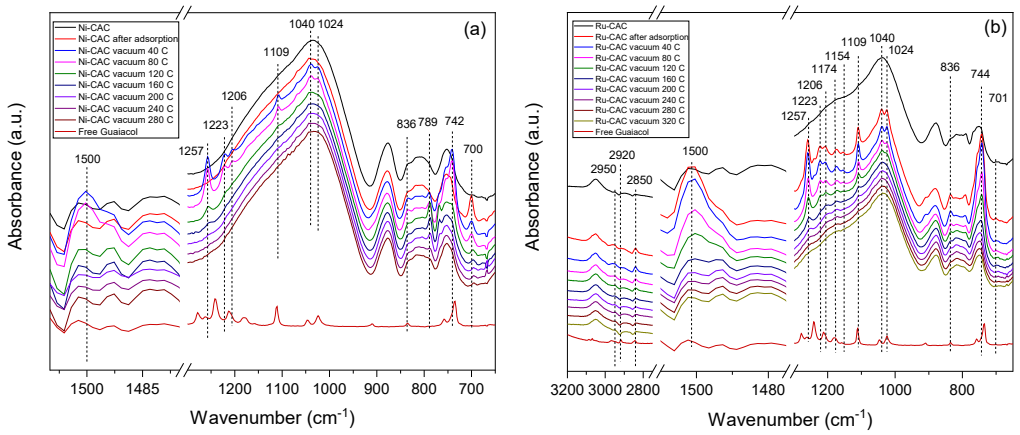

Figure 6: DRIFTS spectra of guaiacol adsorption on (a) Ni-CAC and (b) Ru-CAC. Both Ru-CAC and Ni-CAC show the characteristic peaks of guaiacol at 1500, 1257, and 743 cm^{-1}, which disappear gradually as the temperature is increased, indicating desorption of guaiacol from the catalysts. Free guaiacol represents gaseous guaiacol absent of adsorbate.

For Ru-CAC, the characteristic peaks of guaiacol at 1500, 1257, and 742 cm^{-1} were stronger than those for Ni-CAC, suggesting a stronger adsorption of guaiacol on Ru-CAC than Ni-CAC. Additional peaks at 2850, 2920, and 2950 cm^{-1} were also observed, which were attributed to the C-H vibration of the methyl group. This indicates that the interaction between guaiacol and Ru-CAC was not limited to the catalyst-aromatic ring connection: the catalyst-methyl group interaction was also possible. Spectra for pure guaiacol at 40 °C and 80 °C were also collected for reference, which are shown in Supplementary Information Figure S6. NIST FTIR spectra of guaiacol, cyclohexanol, and cyclohexane are also available in the Supplementary Information and are shown in Supplementary Information Figures S7, S8, and S9, respectively.

After studying the adsorption of guaiacol on the catalysts, we continued by studying the adsorption of guaiacol during the HDO reactions. For the aqueous-phase HDO reactions, the catalysts were retrieved at approximately 50% of the final reaction conversion and at the end of the reaction (100% conversion or 120 min). After drying at 80 °C for 24 h, the catalysts were characterized by DRIFTS, ex situ. It is important to note that some adsorbed species with lower boiling points may be lost during drying of the catalyst. The results for Ni-CAC and Ru-CAC are shown in Figure 7, panels (a)-(b)

and (c)-(d), respectively. At 50% of final conversion, Ni-CAC showed very strong adsorption of guaiacol based on the characteristic peaks at 1500, 1257, and 742 cm^{-1}, which were stronger than in the in-situ adsorption experiment. The band at 2850 to 2950 cm^{-1} was also present, indicating the interaction between the methyl group and the catalyst. After 120 min of reaction, the intensity of characteristic peaks of guaiacol became even stronger, suggesting that more guaiacol was adsorbed at this time than earlier in the reaction.

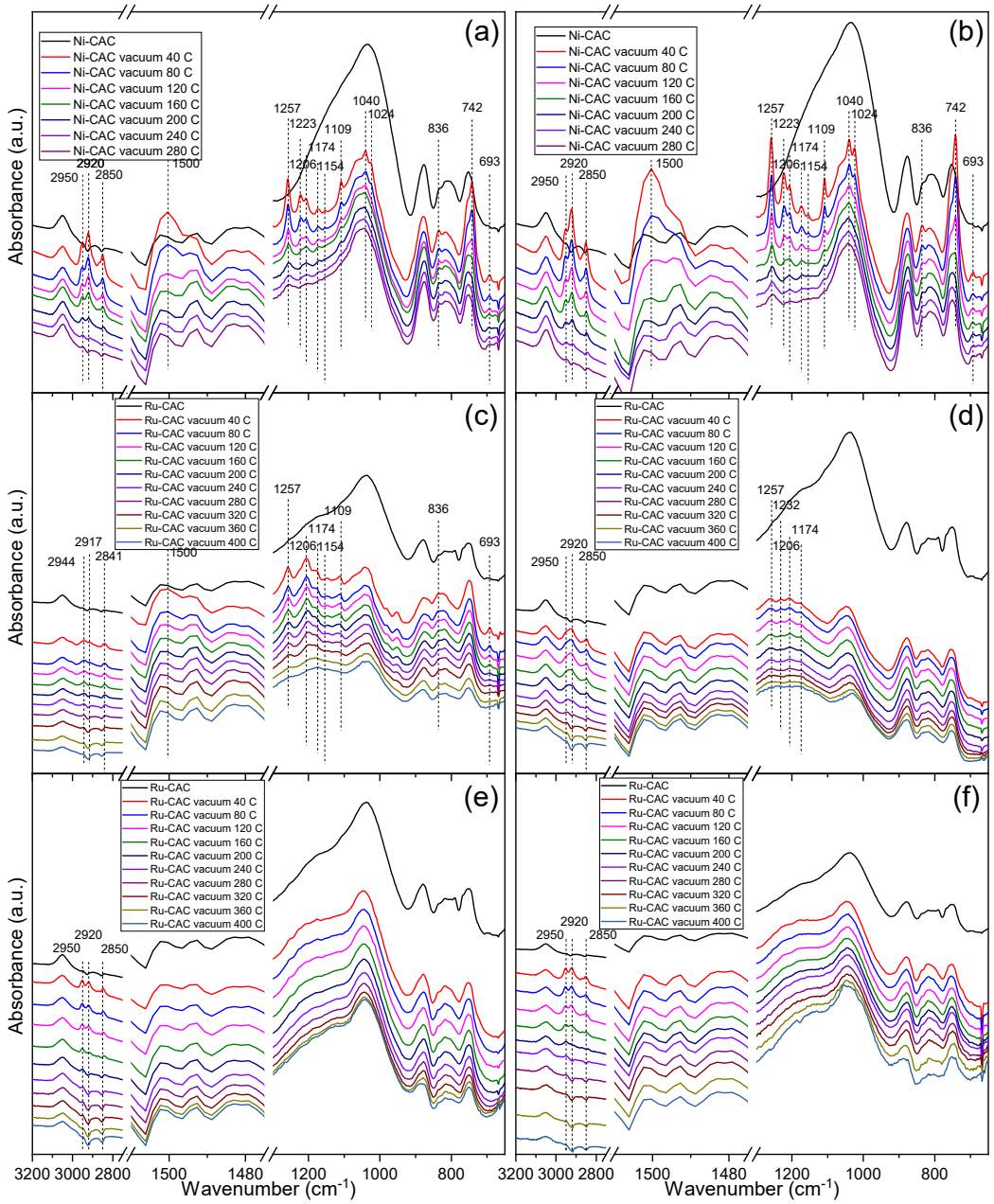

Figure 7: DRIFTS spectra of (a)-(b) Ni-CAC collected in the aqueous-phase reaction at (a) 50% conversion and (b) the end of the reaction; (c)-(d) Ru-CAC collected in the aqueous-phase reaction at (c) 50% conversion and (d) the end of the reaction; and (e)-(f) Ru-CAC collected in the organic-phase reaction at (e) 50% conversion and (f) the end of the reaction. The intensities of the peaks at 1500, 1257, and 743 cm^{-1} indicate that more guaiacol is adsorbed on Ni-CAC as the reaction proceeds, whereas very little guaiacol is adsorbed during the reaction for either of the Ru-CAC experiments.

Ru-CAC samples were retrieved at 5 min and 40 min of reaction due to the high reaction rate in the aqueous phase. For the sample taken at the 5-minute mark, most of the characteristic peaks of guaiacol were very weak or nonexistent. After 40 min of reaction, the peaks at 1500 and 742 cm^{-1} had completely disappeared, suggesting complete conversion of guaiacol, whereas the intensity of the bands at 2850 to 2950 cm^{-1} had increased, most likely due to the formation of products on the catalyst surface that did not desorb. Considering that the main product of this reaction was cyclohexanol, the bands from 2850 to 2950 cm^{-1} were assigned to the C-H bonds of methylene in the cyclic ring of cyclohexanol. Thus, in the aqueous-phase HDO reaction of guaiacol catalyzed by Ru-CAC, we suggest that the origin of the carbon loss was the initial adsorption of guaiacol, and then towards the end of the reaction, the low carbon balance was due to the non-desorption of cyclohexanol rather than guaiacol.

To compare the adsorption phenomena in aqueous- and organic-phase reactions, we conducted the same investigation for Ru-CAC with decane as the solvent. Catalyst samples were collected at 20 min (50% of final conversion) and 120 min (end of reaction), and the resulting DRIFTS spectra are shown in Figure 7, panels (e)-(f). Interestingly, no peaks were found in the low-wavenumber range where most of the characteristic peaks of guaiacol should appear. Several peaks were observed at approximately 2850, 2920 and 2950 cm^{-1}, which are attributed to the C-H bonds of methylene groups. Considering that the solvent in the organic-phase reaction was decane, which should present as C-H bonds under FTIR, and given the absence of other guaiacol peaks, we attribute these peaks to decane adsorbed on the catalyst rather than guaiacol or other products. Additionally, the desorption temperature of these peaks was approximately 200 °C, which was lower than the desorption temperature (240 °C) of similar peaks that were attributed to guaiacol.

Based on this analysis, the adsorption of guaiacol and products such as cyclohexanol on the catalysts should be the main reason for the apparent decrease of carbon in the aqueous-phase reactions. AC-based catalysts may have difficulty desorbing these species in water. This is likely because AC is an organic material and has a high affinity to organic compounds, whereas water, as a polar chemical, has low affinity to organic compounds. Thus, in the aqueous-phase reaction, the adsorption-desorption equilibrium on AC favors the adsorption side, causing the low carbon balance. Due to the low material balance in the aqueous solvent, the calculated rates and kinetic parameters for those HDO reactions should be considered with caution.

3.6. Kinetic Calculations and Reaction Mechanism

Following characterization, the data were passed to the optimization formulation described in Section 2.6. For each catalyst and solvent condition, only reactions whose reactants and products both appeared in the gathered data were considered. The effective rate constants were then determined for the remaining reactions. The model fits for each catalyst in decane and water are presented in Figures 8 and 9, respectively. Generally, although the model-calculated species concentrations do not exactly trace the experimentally determined values over the full reaction time, the fit is usually within a single standard deviation of the experimentally determined value. Given the assumptions in the model formulation and the use of the fits as a qualitative assessment of the likely reaction pathways rather than exact measurements of the reaction kinetics, the closeness of the fits to the experimental data is a positive result. Additionally, it is important to note that the plotted error bars represent the standard deviation of three replicate measurements and do not account for any error in measurement or calibration that may be present. Thus, small deviations outside the presented error bars do not necessarily imply an inadequate model. The complete tables of the kinetic parameters obtained by applying the RIS algorithm to catalysts with decane and water as solvents are presented in the Supplementary Information as Tables S2 and S3, respectively.

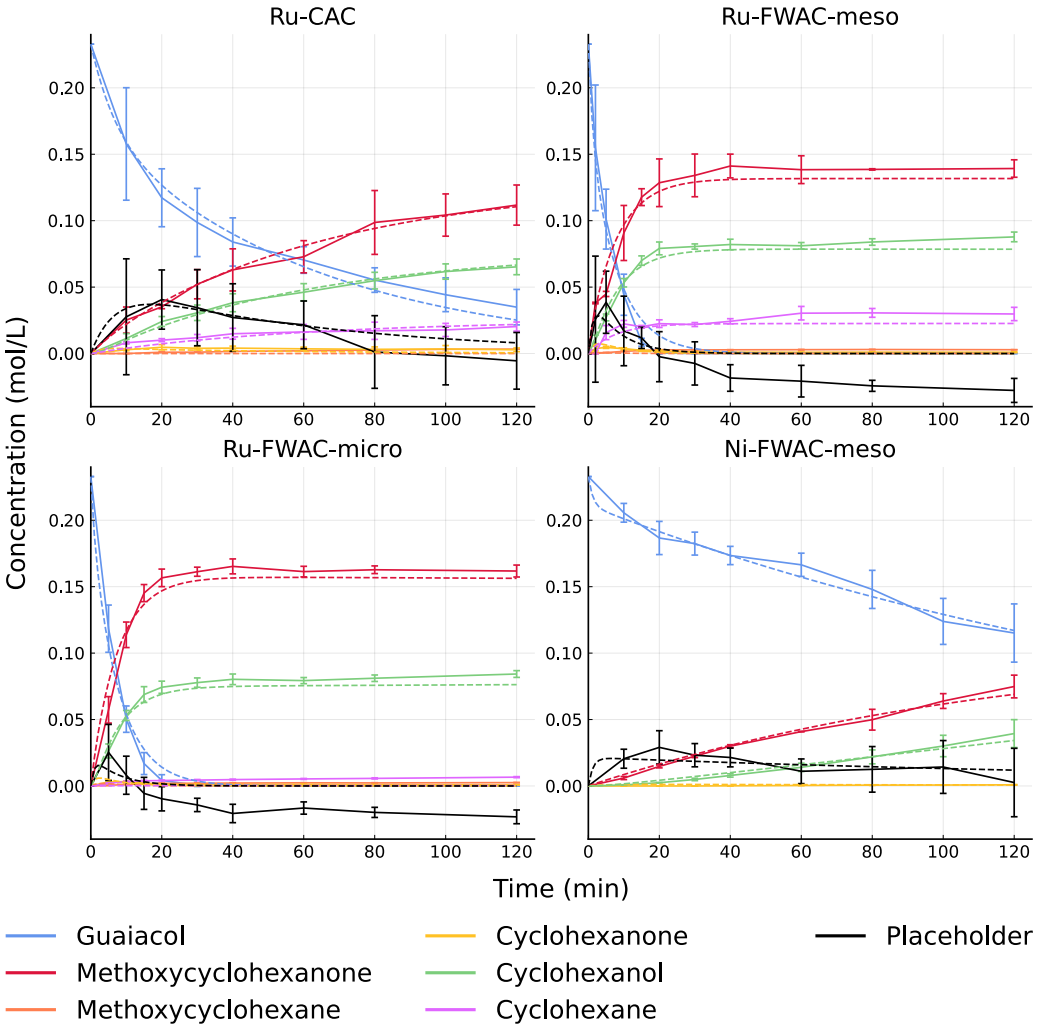

Figure 8: Model-predicted state trajectories (dashed) are plotted against the experimental data (solid) for all catalysts with decane as the solvent. The optimized rate constants provide a reasonable approximation of the experimental data, which is often within one standard deviation (bars) of the gathered data.

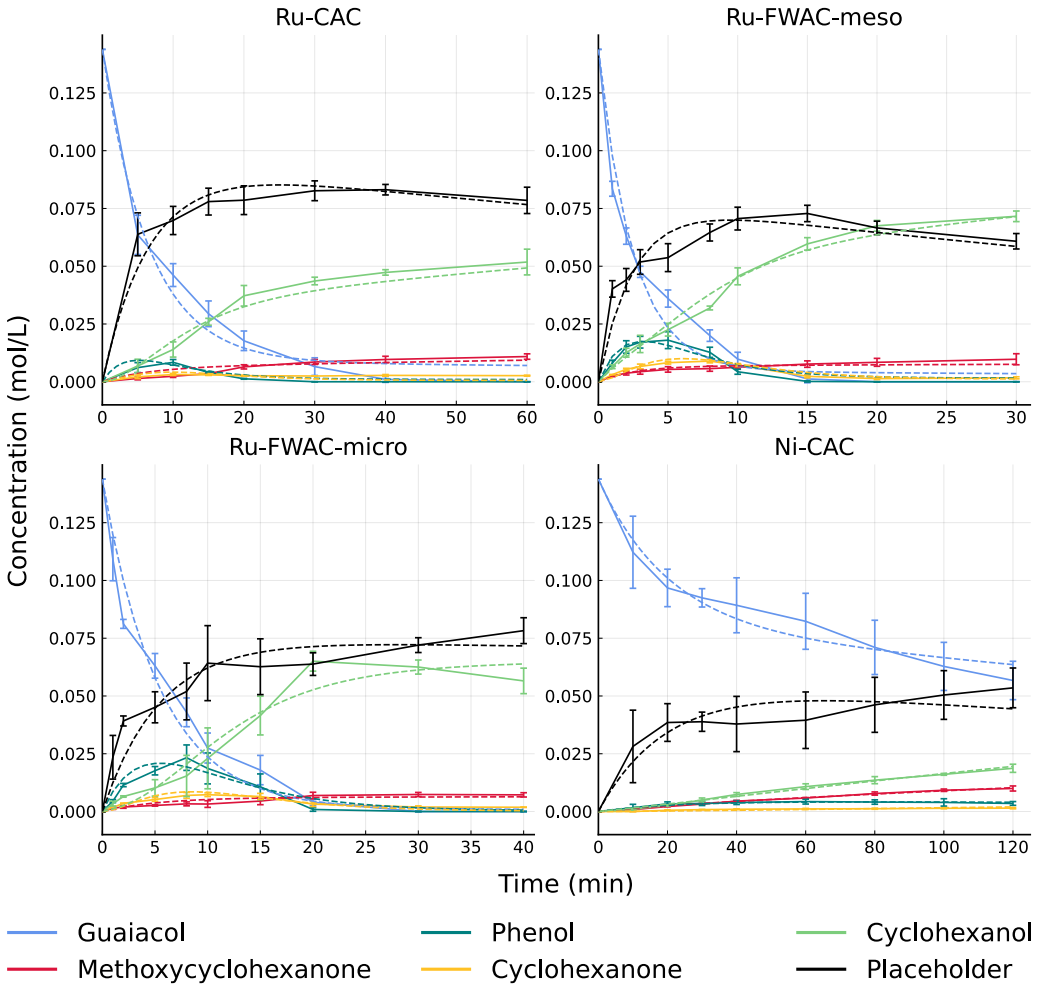

Figure 9: Model-predicted state trajectories (dashed) are plotted against the experimental data (solid) for all catalysts with water as the solvent. The optimized rate constants provide a reasonable approximation of the experimental data, which is often within one standard deviation (bars) of the gathered data.

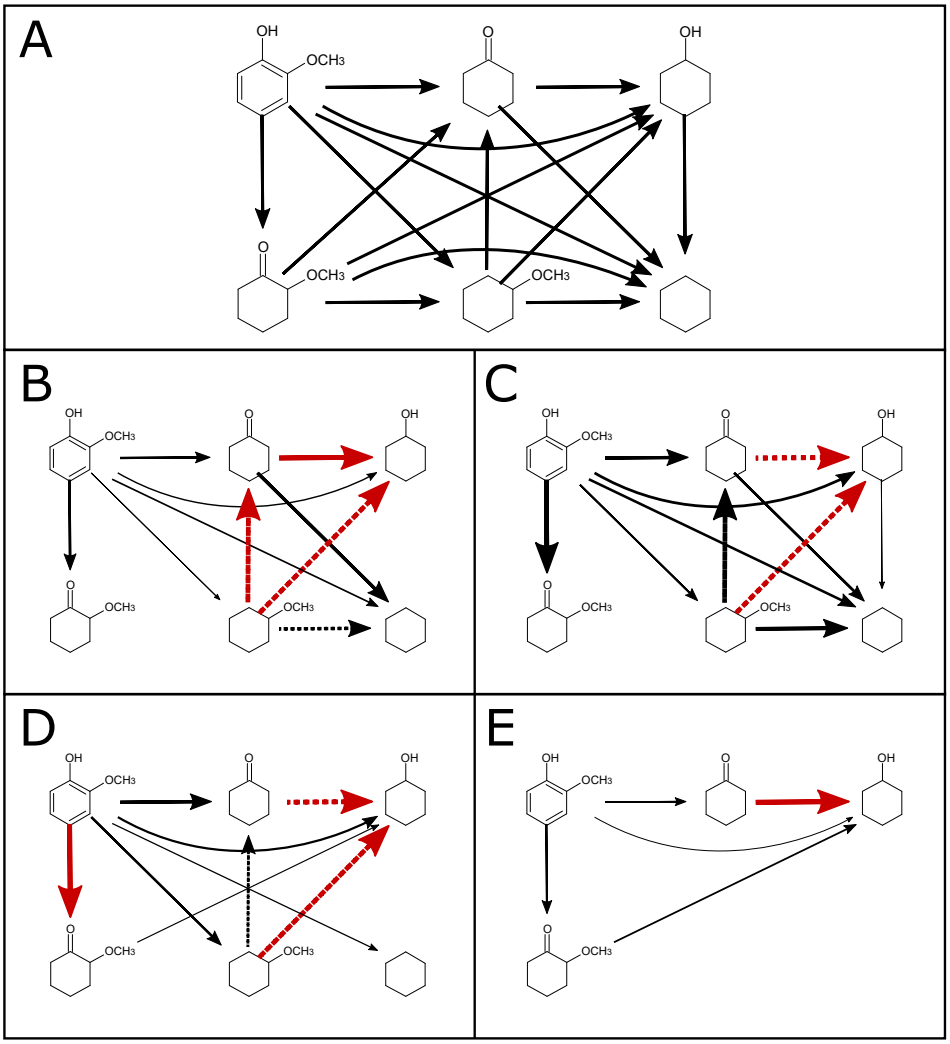

Figure 10: (**A**) The complete reaction pathway from guaiacol to other species found in the HDO reaction with decane as a solvent. Irreversible reactions from every species to each less complicated species are included. Other sections of this figure represent the pathways identified through optimization for the (**B**) Ru-CAC; (**C**) Ru-FWAC-meso; (**D**) Ru-FWAC-micro; and (**E**) Ni-FWAC-meso catalysts. The thicknesses of the black lines for each reaction are set proportional to $-1/\log_{10}(k_{\text{eff}})$. The red lines represent reactions with effective rate constants greater than 0.1 min^{-1}. Lines are not present for reactions with effective rate constants less than 1.0×10^{-6} min^{-1}. Dotted lines indicate reactions whose rates did not greatly affect the model fit according to the sensitivity analysis. The species present include guaiacol (top left molecule), methoxycyclohexanone (bottom left molecule), cyclohexanol (top center molecule), methoxycyclohexanol (bottom center molecule), cyclohexanol (top right molecule), and cyclohexane (bottom right molecule).

Beginning with the optimization results for the catalysts tested in decane, the optimized rate constants presented in Supplementary Information Table S2 of the Supplementary Information were used to construct the reaction pathways shown in Figure 10. Panel (A) shows the complete set of reaction paths that were presented to the optimizer; i.e., each arrow represents a reaction whose effective rate constant the optimizer could adjust to match the model to the gathered kinetic data. The effective rate constants present in Supplementary Information Table S2 were used to determine the thickness of each line in panels (B) through (E), representing the Ru-CAC, Ru-FWAC-meso, Ru-FWAC-micro, and Ni-FWAC-meso catalysts, respectively. Specifically, no lines are shown for very slow reactions—those whose effective rate constants were below 10^{-6} min^{-1}—black lines are shown for reactions with intermediate effective rate constants with thicknesses proportional to $-1/\log_{10}(k_{\text{eff}})$, and red lines represent fast reactions whose effective rate constants were above 10^{-1} min^{-1}. In addition, sensitivity analyses were conducted to determine how sensitive the model is to each effective rate constant. A high sensitivity would indicate that changing the value of the parameter by a small amount may have a substantial impact on the model fit, and a low sensitivity would mean that the value can vary within an order of magnitude without strongly impacting the model. For reactions where the sensitivity analysis indicated a low model sensitivity, below 10^{-5} mol-min/L, the reaction is shown as a dotted line. Based on this visualization, several key points about the decane-solvated pathway can be understood:

- For all four catalysts, the most dominant reaction of guaiacol (top left molecule) is the formation of methoxycyclohexanone (bottom left molecule). This can be seen in Figure 10 by the higher relative thickness of the reaction pathway lines that go from guaiacol to methoxycyclohexanone, compared to those that go from guaiacol to other intermediate species. For the Ru-CAC and Ru-FWAC-meso catalysts (panels (B) and (C), respectively), this was effectively an end point of the reaction: methoxycyclohexanone, once desorbed from the catalyst, did not readsorb and react further to form any other product in any appreciable amount. For the Ru-FWAC-micro and Ni-FWAC-meso catalysts (panels (D) and (E), respectively), optimization revealed a slow-to-moderate rate of reaction for the conversion of methoxycyclohexanone directly to cyclohexanol.

- Although the optimization showed no reaction from methoxycyclo-

hexanone to methoxycyclohexane (bottom center molecule), a small amount of methoxycyclohexane was observed experimentally for the Ru-based catalysts. From the kinetic modeling, the methoxycyclohexane appears to be a direct product of guaiacol. Unlike the non-reactivity of methoxycyclohexanone, the reactivity of methoxycyclohexane is calculated to be much higher, resulting in the formation of both cyclohexanone (top center molecule) and cyclohexanol (top right molecule), and for Ru-CAC and Ru-FWAC-meso, cyclohexane (bottom right molecule). These high effective rate constants are consistent with the small amount of methoxycyclohexane observed in the kinetic data.

- Similarly to methoxycyclohexane, cyclohexanone appears experimentally at very low concentrations for all catalysts tested. The optimization results indicate that this is due to a fast reaction from cyclohexanone to cyclohexanol for all catalysts, and for Ru-CAC and Ru-FWAC-meso, there is also a moderate-speed reaction from cyclohexanone directly to cyclohexane.

- The models for each of the Ru-based catalysts were found to be insensitive to reactions from methoxycyclohexane to cyclohexanone and cyclohexanol. Additionally, for Ru-FWAC-meso and Ru-FWAC-micro, the models were found to be insensitive to the reaction from cyclohexanone to cyclohexanol. This does not mean that these reactions are unimportant to the models, but rather this is indicative of uncertainty regarding the specific reaction rates. Based on the fast rates identified for these reactions, there may be a competitive aspect in which the model is sure that cyclohexanol is being produced but unsure about the degree to which each path is utilized. That is, these reactions were all found to be fast, so both paths are likely to occur quickly, but their exact rates are unclear based on the available data.

- A pathway that seemed likely prior to the optimization analysis was a path from cyclohexanone, through cyclohexanol, and to cyclohexane, in the presence of Ru. However, the optimization indicates that once cyclohexanol is produced, practically none of it reacts further to form cyclohexane. Only for Ru-FWAC-meso is the effective rate constant high enough to appear in the figure, but with its value of only 1.70×10^{-5} min^{-1}, this pathway can only be a minor contributor to the observed amount of cyclohexane. Instead, the cyclohexane appears

to be a direct product of cyclohexanone and methoxycyclohexane for Ru-CAC and Ru-FWAC-meso, and, for all the Ru-based catalysts, it is also a direct product from guaiacol. That is, guaiacol may be adsorbing onto the catalyst and reacting fully to cyclohexane before desorbing. This appears to be especially important for the Ru-FWAC-micro catalyst, where cyclohexane is not identified as a product of any reaction other than that from guaiacol.

It is also possible that, for Ru-FWAC-micro, the absence of reactions producing cyclohexane is an artifact of apparent violations of mass continuity that were observed experimentally. For Ru-FWAC-meso and Ru-FWAC-micro, the kinetic data showed a net positive mass balance by the end of the experiment, likely due to measurement or calibration error. In an attempt to maintain mass continuity, the model addressed this by underestimating the concentration of the product species methoxycyclohexanone, cyclohexanol, and cyclohexane roughly equally to maintain a low sum-of-squared errors. For Ru-FWAC-meso, this mass continuity adjustment did not represent a significant percentage difference in the final concentrations with respect to the experimental data, but for Ru-FWAC-micro, this small adjustment decreased the already experimentally low concentration of cyclohexane to nearly zero in the model. Therefore, there may be a reaction for Ru-FWAC-micro, which was not observed by the optimizer, that also produced cyclohexane. However, given the low concentration of cyclohexane observed experimentally, if such a reaction is present, its rate is likely low.

- For Ni-FWAC-meso, the reaction pathway is fairly simple. Experimentally, neither methoxycyclohexane nor cyclohexane appear, and the kinetic model predicts two pathways: one through methoxycyclohexanone and one through cyclohexanone. Note that the methoxycyclohexanone pathway does not join the cyclohexanone pathway (i.e., cyclohexanone is not predicted to appear as an intermediate), but it instead acts as a parallel pathway to directly produce cyclohexanol.

To summarize the decane-solvated reaction pathways identified through rate-constant optimization, in general there are three parallel pathways for Ru-based catalysts. First, methoxycyclohexanone is produced directly from guaiacol and does not react further. Second, cyclohexanone is produced directly from guaiacol, which then reacts primarily to form cyclohexanol and

secondarily to cyclohexane. Third, methoxycyclohexane is produced directly from guaiacol and reacts to form cyclohexanone (joins with the second pathway), cyclohexanol, or cyclohexane. Cyclohexanol generally does not react to form cyclohexane, so the three nonreacting end products are, in general, methoxycyclohexanone, cyclohexanol, and cyclohexane. There are two parallel pathways for Ni-FWAC-meso. First, methoxycyclohexanone is produced, which then slowly reacts to form cyclohexanol; and second, cyclohexanone is produced, which reacts quickly to form cyclohexanol. Since the reaction from methoxycyclohexanone to cyclohexanol is relatively slow, most of the cyclohexanol appears to be produced via the cyclohexanone pathway.

Changing the solvent from decane to water results in a drastically different set of reaction pathways. As with the analysis for decane-solvated reactions, the optimized effective rate constants presented in Table S3 of the Supplementary Information were used to construct the reaction pathway visualizations shown in Figure 11. Panel (A) shows the complete set of reaction paths presented to the optimizer, and panels (B) through (E) show the optimized pathways for the Ru-CAC, Ru-FWAC-meso, Ru-FWAC-micro, and Ni-CAC catalysts. As in Figure 10, no lines are shown for reactions with effective rate constants below 10^{-6} min^{-1}, black lines are shown for intermediate-speed reactions with thicknesses proportional to $-1/\log_{10}(k_{\text{eff}})$, and red lines are given for reactions with effective rate constants above 0.1 min^{-1}. Any reactions for which the sensitivity analysis indicated a low model sensitivity are presented as dotted lines instead of solid. The key points of Figure 11 are as follows:

- Unlike in the decane-solvated pathways, where the most dominant product from a guaiacol reaction was methoxycyclohexanone, in the water-solvated pathways for every tested catalyst, phenol (top center molecule) was the most dominant immediate product. However, some methoxycyclohexanone is still produced for every catalyst, and much like in the decane pathways, methoxycyclohexanone is usually an end point of the reaction. Only for Ru-FWAC-meso was any appreciable reaction identified from methoxycyclohexanone; for all other catalysts, the rate constant optimization suggests that no further reactions take place.

- As mentioned previously, the most dominant immediate product of the catalytic reaction of guaiacol is phenol, which does not appear

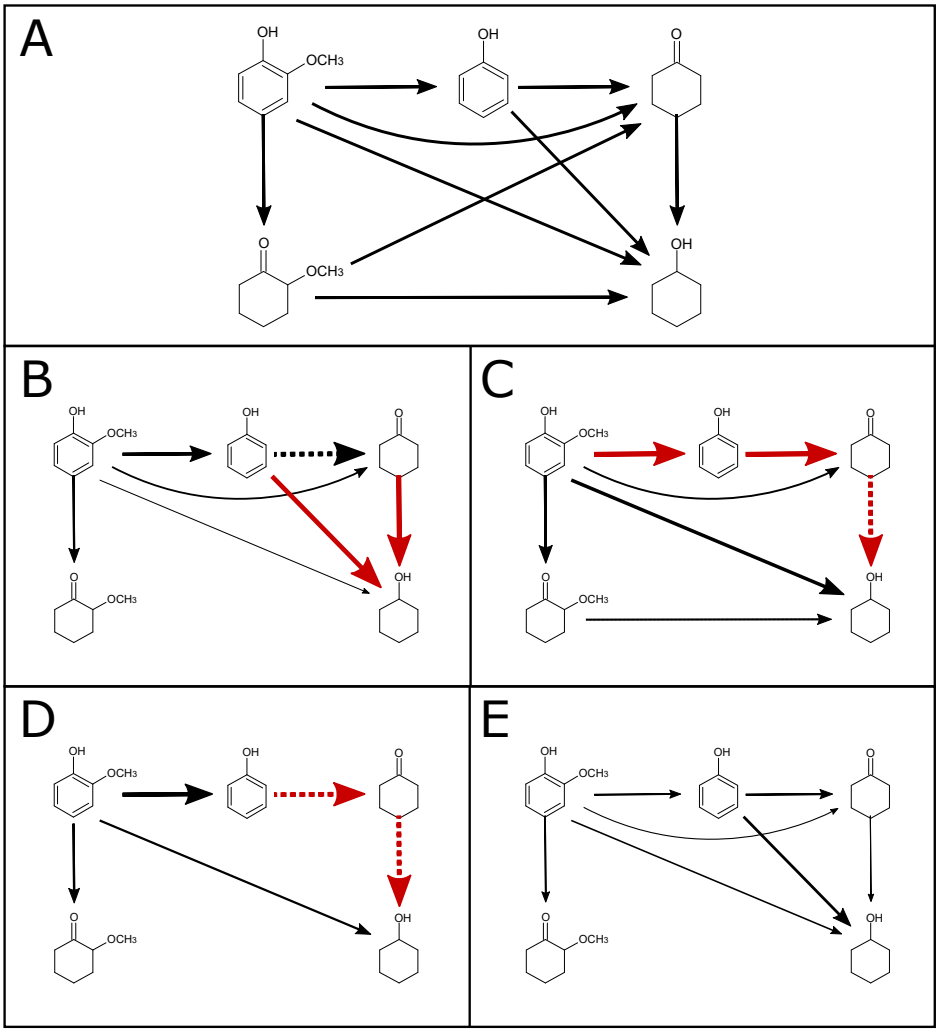

Figure 11: (**A**) The complete reaction pathway from guaiacol to other species found in the HDO reaction with water as a solvent. Irreversible reactions from every species to each less complicated species are included. Other sections of this figure represent the pathways identified through optimization for the (**B**) Ru-CAC; (**C**) Ru-FWAC-meso; (**D**) Ru-FWAC-micro; and (**E**) Ni-CAC catalysts. The thicknesses of the black lines for each reaction are set proportional to $-1/\log_{10}(k_{\text{eff}})$. The red lines represent reactions with effective rate constants greater than 0.1 min^{-1}. Lines are not present for reactions with effective rate constants less than 1.0×10^{-6} min^{-1}. Dotted lines indicate reactions whose rates did not greatly affect the model fit according to the sensitivity analysis. The species present include guaiacol (top left molecule), methoxycyclohexanone (bottom left molecule), phenol (center molecule), cyclohexanone (top right molecule), and cyclohexanol (bottom right molecule).

experimentally in any of the decane-solvated trials. For the three Ru-based catalysts, the kinetics data show that the concentration of phenol peaks early in the reaction and then returns to zero before the end of the experiment. This is consistent with the moderate-to-high effective rate constants identified for the production of phenol from guaiacol—if these rates were too low, the early peak would not appear—and with the high effective rate constants from phenol to cyclohexanone or cyclohexanol, above 0.1 min^{-1} for each Ru catalyst, which must necessarily be fast to bring the phenol concentration back to zero by the end of the experiment.

- Similar to the low amounts of cyclohexanone observed in the decane experiments, a consistently low amount of cyclohexanone was observed in the water experiments. For the Ru-based catalysts, the optimizer suggested a high reaction rate from cyclohexanone to cyclohexanol as the explanation most consistent with the data. For Ni-CAC, the reaction from cyclohexanone to cyclohexanol is estimated to be slow, but the reactions from guaiacol and phenol that produce cyclohexanone are also slow; hence, the low overall concentration of cyclohexanone. For Ni-CAC, the comparatively high final concentration of cyclohexanol, compared to the concentrations of other potential products, appears to be due to direct reactions from phenol and guaiacol, as opposed to being the result of a pathway through cyclohexanone.

- For Ru-FWAC-micro, the model was identified through the sensitivity analysis as being relatively insensitive to the reactions to and from cyclohexanone, though both were estimated to be fast. This insensitivity is likely an indication that the pathway itself is occurring quickly, but the rates of each individual step are more uncertain. That is, the data are consistent with this pathway occurring and these reactions being fast, but it is difficult to estimate exactly how quickly cyclohexanone is produced and reacted away.

- For Ru-FWAC-meso, the model was found to be insensitive to the reaction from methoxycyclohexanone to cyclohexanol. It is important to recognize that the other pathways to produce cyclohexanol, namely, the one passing through phenol and the reaction directly from guaiacol, are several orders of magnitude faster than the pathway through methoxycyclohexanone. Therefore, this insensitivity to the model is likely an

indication that some small amount of cyclohexanol is produced through this pathway, but it is fairly insignificant in comparison with the other pathways, and it is unclear precisely how much this pathway is utilized to produce cyclohexanol.

To summarize the water-solvated reaction pathways identified through rate-constant optimization, in general, the Ru-based catalysts have two parallel pathways. First, much like in the decane pathway, methoxycyclohexanone is produced and does not react further—though for Ru-FWAC-meso, it may react slowly to form cyclohexanol. Second, phenol is produced directly from guaiacol, which then reacts to form cyclohexanone, which then quickly reacts to form cyclohexanol. For Ru-CAC specifically, the phenol may also bypass cyclohexanone and react directly to cyclohexanol, which is the dominant pathway for this catalyst. Furthermore, as can be seen in Figure 11, panels (B) through (D), there appears to be a direct reaction from guaiacol to cyclohexanol for all Ru-based catalysts. This may be due to guaiacol fully reacting to cyclohexanol before desorbing, or it could possibly be an artifact of the fast reaction pathway through phenol. In summary, the two nonreacting products are methoxycyclohexanone and cyclohexanol. For Ni-CAC, the pathway is very similar to that seen for Ru-CAC. That is, one pathway produces methoxycyclohexanone as one nonreacting product, and the other pathway is the reaction of guaiacol to form phenol, which then primarily reacts to directly form cyclohexanol. The difference for Ni-CAC is that any cyclohexanone produced as a secondary product from phenol does not react quickly to form cyclohexanol, as it does for the Ru-based catalysts. The consequence of this is that should the reaction continue for an extended period of time, there should be a total of three products that are nearly nonreactive: methoxycyclohexanone, cyclohexanol, and cyclohexanone.

Previous computational studies have provided valuable insights into guaiacol HDO pathways. Saleheen *et al.*[54] investigated the pathway on Ru(0001) demonstrating that it favored the production of phenol as an intermediate product followed by ring hydrogenation. Their study on different solvents (water, 1-butanol, diethyl ether, and hexane) concluded that the phenol pathway was most favorable regardless of the solvent environment.[54] For Ni(111) surfaces, Morteo-Flores *et al.*[55] found that the most favorable pathway involves the formation of catechol followed by phenol, then hydrogenolysis to benzene. Our experimental results and kinetic analysis align with these DFT predictions, in which phenol is observed as the primary intermediate when

water is the solvent. However, our experimental results showed that in the decane-solvated reactions the dominant reaction product was methoxycyclohexanone, suggesting that in nonpolar organic solvents the most favorable reaction pathway is not through a phenol intermediate.

4. Conclusions

This work highlights the importance of solvents, metals, and carbon supports on the liquid-phase HDO reactions of bio-oils. AC supports with different properties such as porosity, hydrophobicity, and morphology, derived from fossil or renewable resources, were impregnated with Ru or Ni. The prepared materials were then calcined, reduced, and used as catalysts for the HDO of guaiacol in the liquid phase using either water or decane as the solvent.

The results revealed the impacts of different catalyst features on their activities in the HDO reaction of guaiacol. For the active phase, the Ru-based catalysts were found to be more active than the Ni-based catalysts. For the AC support, having a higher mesoporosity was beneficial, as it led to higher metal dispersion and therefore to higher catalyst activity. AC hydrophobicity also played a role, as the more hydrophilic CAC support showed better performance in the aqueous reactions than in the decane reactions. The choice of solvent also affected the reaction pathway and product selectivity. Nonpolar products, such as cyclohexane and methoxycyclohexane, were formed only in the organic-phase reaction and were prohibited in water. More polar products, such as phenol and cyclohexanol, were favored in the aqueous-phase reactions. Furthermore, the use of water as a solvent resulted in a poor carbon balance during the experiments. In-situ DRIFTS analysis revealed that the loss of carbon balance is due to the adsorption of guaiacol or products on the catalysts. In the aqueous phase, the AC support may have difficulty desorbing organic compounds, which may remain on the surface of the AC, leading to a negative carbon balance in the liquid phase. Most importantly, when Ru was used as the active phase, the FWAC-supported catalysts were much more active than the CAC-supported catalyst. This result shows that AC derived from food waste has excellent potential as a catalyst support, making the HDO reaction a complete renewable process. Finally, modeling efforts revealed several important features of the reaction pathways, such as the relative nonreactivity of methoxycyclohexanone and that cyclohexanol was not found to be an intermediate species in the production of cyclohex-

ane. Data-driven analysis, such as that used in this paper, is thus a cheap but effective tool that can provide unique insight into catalytic reactions of interest.

Acknowledgments

Funding: This work was supported by the University of Connecticut, Office of the Vice President for Research (OVPR), Research Excellence Program (REP).

Data Availability

The data in this article and the code used for kinetic mechanism analyses are available at the following public GitHub repository: `https://github.com/PSORLab/HDO_Data_Analysis`.

References

[1] D. Raikwar, M. Munagala, S. Majumdar and D. Shee, *Catalysis Today*, 2019, **325**, 117–130, DOI: 10.1016/j.cattod.2018.09.039.

[2] S. Cheng, L. Wei, X. Zhao, E. Kadis, Y. Cao, J. Julson and Z. Gu, *New Biotechnology*, 2016, **33**, 440–448, DOI: 10.1016/j.nbt.2016.02.004.

[3] L. Yu, A. Farinmade, O. Ajumobi, V. T. John and J. A. Valla, *Energy & Fuels*, 2021, **35**, 20117–20130, DOI: 10.1021/acs.energyfuels.1c02453.

[4] D. Singh and P. L. Dhepe, *Molecular Catalysis*, 2020, **480**, 110525, DOI: 10.1016/j.mcat.2019.110525.

[5] E. Blanco, C. Sepulveda, K. Cruces, J. García-Fierro, I. Ghampson and N. Escalona, *Catalysis Today*, 2020, **356**, 376–383, DOI: 10.1016/j.cattod.2019.08.029.

[6] D. P. Gamliel, S. Karakalos and J. A. Valla, *Applied Catalysis A: General*, 2018, **559**, 20–29, DOI: 10.1016/j.apcata.2018.04.004.

[7] D. P. Gamliel, G. M. Bollas and J. A. Valla, *Fuel*, 2018, **216**, 160–170, DOI: 10.1016/j.fuel.2017.12.017.

[8] L. Yu, A. Farinmade, O. Ajumobi, Y. Su, V. T. John and J. A. Valla, *Applied Catalysis A: General*, 2020, **602**, 117727, DOI: 10.1016/j.apcata.2020.117727.

[9] D. P. Gamliel, S. Du, G. M. Bollas and J. A. Valla, *Bioresource Technology*, 2015, **191**, 187–196, DOI: 10.1016/j.biortech.2015.04.129.

[10] H. V. Ly, E. Galiwango, S.-S. Kim, J. Kim, J. H. Choi, H. C. Woo and M. R. Othman, *Chemical Engineering Journal*, 2017, **317**, 302–308, DOI: 10.1016/j.cej.2017.02.080.

[11] Z. Li, E. Jiang, X. Xu, Y. Sun and R. Tu, *Renewable Energy*, 2020, **146**, 1991–2007, DOI: 10.1016/j.renene.2019.08.012.

[12] D. P. Gamliel, B. P. Baillie, E. Augustine, J. Hall, G. M. Bollas and J. A. Valla, *Microporous and Mesoporous Materials*, 2018, **261**, 18–28, DOI: 10.1016/j.micromeso.2017.10.027.

[13] Y. He, Y. Bie, J. Lehtonen, R. Liu and J. Cai, *Fuel*, 2019, **239**, 1015–1027, DOI: 10.1016/j.fuel.2018.11.103.

[14] H. Fang, J. Zheng, X. Luo, J. Du, A. Roldan, S. Leoni and Y. Yuan, *Applied Catalysis A: General*, 2017, **529**, 20–31, DOI: 10.1016/j.apcata.2016.10.011.

[15] V. Yakovlev, S. Khromova, O. Sherstyuk, V. Dundich, D. Ermakov, V. Novopashina, M. Lebedev, O. Bulavchenko and V. Parmon, *Catalysis Today*, 2009, **144**, 362–366, DOI: 10.1016/j.cattod.2009.03.002.

[16] T. Nimmanwudipong, R. C. Runnebaum, D. E. Block and B. C. Gates, *Catalysis Letters*, 2011, **141**, 779–783, DOI: 10.1007/s10562-011-0576-4.

[17] H. Zhao, D. Li, P. Bui and S. Oyama, *Applied Catalysis A: General*, 2011, **391**, 305–310, DOI: 10.1016/j.apcata.2010.07.039.

[18] P. M. Mortensen, H. W. de Carvalho, J.-D. Grunwaldt, P. A. Jensen and A. D. Jensen, *Journal of Catalysis*, 2015, **328**, 208–215, DOI: 10.1016/j.jcat.2015.02.002.

[19] X. Zhang, P. Yan, B. Zhao, K. Liu, M. C. Kung, H. H. Kung, S. Chen and Z. C. Zhang, *ACS Catalysis*, 2019, **9**, 3551–3563, DOI: 10.1021/acscatal.9b00400.

[20] R. Shu, B. Lin, J. Zhang, C. Wang, Z. Yang and Y. Chen, *Fuel Processing Technology*, 2019, **184**, 12–18, DOI: 10.1016/j.fuproc.2018.11.004.

[21] S. Ahmadi, Z. Yuan, S. Rohani and C. C. Xu, *Catalysis Today*, 2016, **269**, 182–194, DOI: 10.1016/j.cattod.2015.08.040.

[22] A. Sulman, P. Mäki-Arvela, L. Bomont, V. Fedorov, M. Alda-Onggar, A. Smeds, J. Hemming, V. Russo, J. Wärnå, M. Käldström and D. Y. Murzin, *Catalysis Letters*, 2018, **148**, 2856–2868, DOI: 10.1007/s10562-018-2478-1.

[23] X. Xu and E. Jiang, *Energy & Fuels*, 2017, **31**, 2855–2864, DOI: 10.1021/acs.energyfuels.6b02700.

[24] A. Maia, B. Louis, Y. Lam and M. Pereira, *Journal of Catalysis*, 2010, **269**, 103–109, DOI: 10.1016/j.jcat.2009.10.021.

[25] X. Zhu, L. L. Lobban, R. G. Mallinson and D. E. Resasco, *Journal of Catalysis*, 2011, **281**, 21–29, DOI: 10.1016/j.jcat.2011.03.030.

[26] X. Xu, E. Jiang, Y. Du and B. Li, *Renewable Energy*, 2016, **96**, 458–468, DOI: 10.1016/j.renene.2016.04.094.

[27] C. Sepúlveda, R. García, P. Reyes, I. Ghampson, J. Fierro, D. Laurenti, M. Vrinat and N. Escalona, *Applied Catalysis A: General*, 2014, **475**, 427–437, DOI: 10.1016/j.apcata.2014.01.057.

[28] J. Sun, A. M. Karim, H. Zhang, L. Kovarik, X. S. Li, A. J. Hensley, J.-S. McEwen and Y. Wang, *Journal of Catalysis*, 2013, **306**, 47–57, DOI: 10.1016/j.jcat.2013.05.020.

[29] K. B. Jung, J. Lee, J.-M. Ha, H. Lee, D. J. Suh, C.-H. Jun and J. Jae, *Catalysis Today*, 2018, **303**, 191–199, DOI: 10.1016/j.cattod.2017.07.027.

[30] V. Ranaware, D. Verma, R. Insyani, A. Riaz, S. M. Kim and J. Kim, *Green Chemistry*, 2019, **21**, 1021–1042, DOI: 10.1039/c8gc03623c.

[31] E. Santillan-Jimenez, M. Perdu, R. Pace, T. Morgan and M. Crocker, *Catalysts*, 2015, **5**, 424–441, DOI: 10.3390/catal5010424.

[32] H. Purón, J. Pinilla, I. Suelves and M. Millan, *Catalysis Today*, 2015, **249**, 79–85, DOI: 10.1016/j.cattod.2014.09.021.

[33] S. Liu, H. Wang, K. J. Smith and C. S. Kim, *Energy & Fuels*, 2017, **31**, 6378–6388, DOI: 10.1021/acs.energyfuels.7b00452.

[34] H. Shafaghat, P. S. Rezaei and W. M. A. W. Daud, *RSC Advances*, 2015, **5**, 103999–104042, DOI: 10.1039/c5ra22137d.

[35] T. Sankaranarayanan, M. Kreider, A. Berenguer, S. Gutiérrez-Rubio, I. Moreno, P. Pizarro, J. Coronado and D. Serrano, *Fuel*, 2018, **214**, 187–195, DOI: 10.1016/j.fuel.2017.10.059.

[36] J. Matthiesen, T. Hoff, C. Liu, C. Pueschel, R. Rao and J.-P. Tessonnier, *Chinese Journal of Catalysis*, 2014, **35**, 842–855, DOI: 10.1016/s1872-2067(14)60122-4.

[37] P. Sirous-Rezaei, J. Jae, K. Cho, C. H. Ko, S.-C. Jung and Y.-K. Park, *Chemical Engineering Journal*, 2019, **377**, 120121, DOI: 10.1016/j.cej.2018.10.058.

[38] A. Berenguer, J. A. Bennett, J. Hunns, I. Moreno, J. M. Coronado, A. F. Lee, P. Pizarro, K. Wilson and D. P. Serrano, *Catalysis Today*, 2018, **304**, 72–79, DOI: 10.1016/j.cattod.2017.08.032.

[39] E. Lam and J. H. Luong, *ACS Catalysis*, 2014, **4**, 3393–3410, DOI: 10.1021/cs5008393.

[40] A. A. Dwiatmoko, L. Zhou, I. Kim, J.-W. Choi, D. J. Suh and J.-M. Ha, *Catalysis Today*, 2016, **265**, 192–198, DOI: 10.1016/j.cattod.2015.08.027.

[41] H. Shafaghat, J. M. Kim, I.-G. Lee, J. Jae, S.-C. Jung and Y.-K. Park, *Renewable Energy*, 2019, **144**, 159–166, DOI: 10.1016/j.renene.2018.06.096.

[42] S. Oh, J. H. Lee and J. W. Choi, *Renewable Energy*, 2020, **160**, 1160–1167, DOI: 10.1016/j.renene.2020.07.051.

[43] T. Cordero-Lanzac, J. Rodríguez-Mirasol, T. Cordero and J. Bilbao, *Energy & Fuels*, 2021, **35**, 17008–17031, DOI: 10.1021/acs.energyfuels.1c01700.

[44] S. Yang, G. Chen, Q. Guan, H. Xu, Z. Wang, B. Liu, S. Yang, T. Lei, X. Zeng and L. Lin, *Molecular Catalysis*, 2021, **510**, 111681, DOI: 10.1016/j.mcat.2021.111681.

[45] D.-P. Phan, V. N. Le, J. Kim and E. Y. Lee, *Fuel Processing Technology*, 2021, **224**, 107001, DOI: 10.1016/j.fuproc.2021.107001.

[46] F. Broglia, L. Rimoldi, D. Meroni, S. D. Vecchi, M. Morbidelli and S. Ardizzone, *Fuel*, 2019, **243**, 501–508, DOI: 10.1016/j.fuel.2019.01.157.

[47] Y. Hong, H. Zhang, J. Sun, K. M. Ayman, A. J. R. Hensley, M. Gu, M. H. Engelhard, J.-S. McEwen and Y. Wang, *ACS Catalysis*, 2014, **4**, 3335–3345, DOI: 10.1021/cs500578g.

[48] S. Alijani, S. Capelli, C. Evangelisti, L. Prati, A. Villa and S. Cattaneo, *Catalysis Today*, 2021, **367**, 220–227, DOI: 10.1016/j.cattod.2020.04.026.

[49] Z. Tian, X. Liang, R. Li, C. Wang, J. Liu, L. Lei, R. Shu and Y. Chen, *Fuel*, 2022, **308**, 122034, DOI: 10.1016/j.fuel.2021.122034.

[50] L. Hu, X.-Y. Wei, M.-L. Xu, Y.-H. Kang, X.-H. Guo, F.-B. Zhang, Z.-M. Zong and H.-C. Bai, *Journal of Environmental Chemical Engineering*, 2021, **9**, 106599, DOI: 10.1016/j.jece.2021.106599.

[51] Y. Jeong, C. W. Park, Y.-K. Park, J.-M. Ha, Y. Jeong, K.-Y. Lee and J. Jae, *Catalysis Today*, 2021, **375**, 164–173, DOI: 10.1016/j.cattod.2020.05.004.

[52] A. Bjelić, M. Grilc, M. Huš and B. Likozar, *Chemical Engineering Journal*, 2019, **359**, 305–320, DOI: 10.1016/j.cej.2018.11.107.

[53] J. Wildschut, F. H. Mahfud, R. H. Venderbosch and H. J. Heeres, *Industrial & Engineering Chemistry Research*, 2009, **48**, 10324–10334, DOI: 10.1021/ie9006003.

[54] M. Saleheen, A. M. Verma, O. Mamun, J. Lu and A. Heyden, *Catalysis Science & Technology*, 2019, **9**, 6253–6273, DOI: 10.1039/c9cy01763a.

[55] F. Morteo-Flores, M. Quayle, A. Salom-Català, M. Pera-Titus and A. Roldan, *ChemCatChem*, 2023, **15**, e202300671, DOI: 10.1002/cctc.202300671.

[56] A. B. Dongil, I. T. Ghampson, R. García, J. L. G. Fierro and N. Escalona, *RSC Advances*, 2016, **6**, 2611–2623, DOI: 10.1039/c5ra22540j.

[57] C. Zhao, J. He, A. A. Lemonidou, X. Li and J. A. Lercher, *Journal of Catalysis*, 2011, **280**, 8–16, DOI: 10.1016/j.jcat.2011.02.001.

[58] C. Zhang, C. Jia, Y. Cao, Y. Yao, S. Xie, S. Zhang and H. Lin, *Green Chemistry*, 2019, **21**, 1668–1679, DOI: 10.1039/c8gc04017f.

[59] J. Qi, X. Sun, S.-F. Tang, Y. Sun, C. Xu, X. Li and X. Li, *Applied Catalysis A: General*, 2017, **535**, 24–31, DOI: 10.1016/j.apcata.2017.01.020.

[60] R. Barton, M. Carrier, C. Segura, J. Fierro, S. Park, H. Lamb, N. Escalona and S. Peretti, *Applied Catalysis A: General*, 2018, **562**, 294–309, DOI: 10.1016/j.apcata.2018.06.012.

[61] L. Yu, D. P. Gamliel, B. Markunas and J. A. Valla, *ACS Omega*, 2021, **6**, 8870–8883, DOI: 10.1021/acsomega.0c06029.

[62] W. H. Green, *AIChE Journal*, 2020, **66**, e17059, DOI: 10.1002/aic.17059.

[63] R. Mahadevan, J. S. Edwards and F. J. Doyle, *Biophysical Journal*, 2002, **83**, 1331–1340, DOI: 10.1016/s0006-3495(02)73903-9.

[64] A. Varma and B. O. Palsson, *Bio/Technology*, 1994, **12**, 994–998, DOI: 10.1038/nbt1094-994.

[65] K. N. Heck, B. G. Janesko, G. E. Scuseria, N. J. Halas and M. S. Wong, *Journal of the American Chemical Society*, 2008, **130**, 16592–16600, DOI: 10.1021/ja803556k.

[66] A. B. Singer, J. W. Taylor, P. I. Barton and W. H. Green, *The Journal of Physical Chemistry A*, 2006, **110**, 971–976, DOI: 10.1021/jp0548873.

[67] F. Caraffini, F. Neri, B. N. Passow and G. Iacca, *Soft Computing*, 2013, **17**, 2235–2256, DOI: 10.1007/s00500-013-1106-7.

[68] A. Stukalov, R. Anantharaman and R. Feldt, *robertfeldt/BlackBoxOptim.jl*, 2021, `https://github.com/robertfeldt/BlackBoxOptim.jl`.

[69] R. Horst and H. Tuy, *Global Optimization: Deterministic Approaches*, Springer Berlin Heidelberg, 2013.

[70] N. V. Sahinidis, *Journal of Global Optimization*, 1996, **8**, 201–205, DOI: 10.1007/bf00138693.

[71] D. Bongartz, J. Najman, S. Sass and A. Mitsos, 2018.

[72] M. E. Wilhelm and M. D. Stuber, *Optimization Methods and Software*, 2020, **37**, 425–450, DOI: 10.1080/10556788.2020.1786566.

[73] J. Bezanson, A. Edelman, S. Karpinski and V. B. Shah, *Julia: A Fresh Approach to Numerical Computing*, 2014, DOI: 10.48550/ARXIV.1411.1607.

[74] I. Sobol, *USSR Computational Mathematics and Mathematical Physics*, 1967, **7**, 86–112, DOI: 10.1016/0041-5553(67)90144-9.

[75] S. G. Johnson, *stevengj/Sobol.jl*, 2020, `https://github.com/stevengj/Sobol.jl`.

[76] Y. bin Tang, Q. Liu and F. yan Chen, *Chemical Engineering Journal*, 2012, **203**, 19–24, DOI: 10.1016/j.cej.2012.07.007.

[77] G. Wang, C. Pan, L. Wang, Q. Dong, C. Yu, Z. Zhao and J. Qiu, *Electrochimica Acta*, 2012, **69**, 65–70, DOI: 10.1016/j.electacta.2012.02.066.

[78] F. Miculescu, G. E. Stan, L. T. Ciocan, M. Miculescu, A. Berbecaru and I. Antoniac, *Dig. J. Nanomater. Biostructures*, 2012, **7**, 1667–1677.

[79] D. J. Suh, P. Tae-Jin and I. Son-Ki, *Carbon*, 1993, **31**, 427–435, DOI: 10.1016/0008-6223(93)90130-3.

[80] M. B. Dawidziuk, F. Carrasco-Marín and C. Moreno-Castilla, *Carbon*, 2009, **47**, 2679–2687, DOI: 10.1016/j.carbon.2009.05.025.

[81] W. Wang, K. Wu, S. Tan and Y. Yang, *ACS Sustainable Chemistry & Engineering*, 2017, **5**, 8602–8609, DOI: 10.1021/acssuschemeng.7b01087.

[82] H. Wan, R. V. Chaudhari and B. Subramaniam, *Topics in Catalysis*, 2012, **55**, 129–139, DOI: 10.1007/s11244-012-9782-6.

[83] J. Shangguan, N. Pfriem and Y.-H. C. Chin, *Journal of Catalysis*, 2019, **370**, 186–199, DOI: 10.1016/j.jcat.2018.11.036.

[84] J. Shangguan, A. J. R. Hensley, M. V. Gradiski, N. Pfriem, J.-S. McEwen, R. H. Morris and Y.-H. C. Chin, *ACS Catalysis*, 2020, **10**, 12310–12332, DOI: 10.1021/acscatal.0c01963.

[85] M. Zhou, J. Ye, P. Liu, J. Xu and J. Jiang, *ACS Sustainable Chemistry & Engineering*, 2017, **5**, 8824–8835, DOI: 10.1021/acssuschemeng.7b01615.

[86] Z. Zheng, Z. Luo and C. Zhao, *ChemCatChem*, 2018, **10**, 1376–1384, DOI: 10.1002/cctc.201701398.

[87] A. Popov, E. Kondratieva, J. M. Goupil, L. Mariey, P. Bazin, J.-P. Gilson, A. Travert and F. Maugé, *The Journal of Physical Chemistry C*, 2010, **114**, 15661–15670, DOI: 10.1021/jp101949j.

[88] X. Wang, S. Zhu, S. Wang, Y. He, Y. Liu, J. Wang, W. Fan and Y. Lv, *RSC Advances*, 2019, **9**, 3868–3876, DOI: 10.1039/c8ra09972c.

Supplementary Information

An Integrated Reaction Model of Guaiacol Hydrodeoxygenation Using Activated Carbon Supports: Effects of Support Properties, Metals, and Solvents

Lei Yu[a,b,1], Robert X. Gottlieb[a,c,1], Jeffrey Page[a,b], Julia A. Valla[a,b,*], Matthew D. Stuber[a,c,*]

[a] *Department of Chemical & Biomolecular Engineering, University of Connecticut, Storrs, 06269, CT, USA*
[b] *Center for Clean Energy Engineering, University of Connecticut, Storrs, 06269 CT, USA*
[c] *Process Systems and Operations Research Laboratory, University of Connecticut, Storrs, 06269, CT, USA*

Keywords: reaction mechanisms, kinetic parameter estimation, renewable resources, mathematical programming, optimization

[*] Co-corresponding authors.
Email addresses: ioulia.valla@uconn.edu (Julia A. Valla), stuber@alum.mit.edu (Matthew D. Stuber)
[1] Authors share co-first authorship.

Table S1: A summary of the conversion x, final product yield Y_i, and carbon balance ξ for guaiacol HDO presented in this work. The primary product of guaiacol HDO in water-solvated reactions was cyclohexanol, and in decane-solvated reactions it was methoxycyclohexanone. Water-solvated reactions show a decrease in CB owing to adsorption of guaiacol onto the catalyst's support. Methanol and methane were not included in the carbon balance calculations, as they were not quantified in this study. (Key: C..ane=cyclohexane, C..ol=cyclohexanol, C..one=cyclohexanone, MC..ane=methoxycyclohexane, MC..one=methoxycyclohexanone)

			Product Yield (%)						
Solvent	Sample	x (%)	C..ane	C..ol	C..one	Phenol	MC..ane	MC..one	ξ (%)
Water	Ni-CAC	60.6	0	13.0	1.0	2.4	0	6.9	57.7
	Ni-FWAC Micro	0	-	-	-	-	-	-	-
	Ni-FWAC Meso	0	-	-	-	-	-	-	-
	Ru-CAC	100	0	36.0	1.8	0	0	7.6	33.9
	Ru-FWAC Micro	100	0	39.3	1.3	0	0	5.0	33.2
	Ru-FWAC Meso	100	0	49.8	1.2	0	0	6.8	42.3
Decane	Ni-CAC	0	-	-	-	-	-	-	-
	Ni-FWAC Micro	0	-	-	-	-	-	-	-
	Ni-FWAC Meso	50.6	0.0	16.9	0.4	0	0	32.1	94.4
	Ru-CAC	85.6	8.7	28.0	1.2	0	1.2	47.9	90.2
	Ru-FWAC Micro	100	2.9	36.2	0.4	0	1.1	69.5	99.7
	Ru-FWAC Meso	100	12.7	37.7	0.4	0	1.2	59.8	96.6

Table S2: Effective rate constants are tabulated by catalyst, with decane as the solvent. Values under 1×10^{-6} are grayed out and assumed to be zero for pathway analysis. Values with asterisks $(*)$ were found to have relatively lower impact on the model fit through a sensitivity analysis. Units are min^{-1}. (Key: C..ane=cyclohexane, C..ol=cyclohexanol, C..one=cyclohexanone, MC..ane=methoxycyclohexane, MC..one=methoxycyclohexanone)

Effective Rate Constant	Ru			Ni
	CAC	FWAC-meso	FWAC-micro	FWAC-meso
Guai → Placeholder	3.07×10^{-2}	1.42×10^{-1}	$9.91 \times 10^{-2}(*)$	7.34×10^{-2}
Placeholder → Guai	1.12×10^{-1}	6.50×10^{-1}	1.00×10^{0}	7.26×10^{-1}
Guai → MC..one	1.16×10^{-2}	9.20×10^{-2}	1.01×10^{-1}	4.16×10^{-3}
Guai → MC..ane	3.35×10^{-6}	3.08×10^{-3}	7.53×10^{-3}	—
Guai → Phenol	—	—	—	—
Guai → C..one	7.32×10^{-3}	3.36×10^{-2}	3.30×10^{-2}	1.26×10^{-3}
Guai → C..ol	4.80×10^{-4}	1.91×10^{-2}	7.35×10^{-3}	3.86×10^{-6}
Guai → C..ane	1.55×10^{-3}	1.48×10^{-2}	2.05×10^{-4}	—
MC..one → MC..ane	3.21×10^{-23}	8.52×10^{-24}	4.40×10^{-23}	—
MC..one → C..one	6.96×10^{-20}	9.14×10^{-22}	6.11×10^{-21}	1.57×10^{-19}
MC..one → C..ol	1.63×10^{-25}	3.85×10^{-22}	7.74×10^{-5}	2.26×10^{-3}
MC..one → C..ane	2.75×10^{-22}	1.41×10^{-24}	1.14×10^{-20}	—
MC..ane → C..one	$7.91 \times 10^{-1}(*)$	$9.68 \times 10^{-2}(*)$	$1.99 \times 10^{-2}(*)$	—
MC..ane → C..ol	$1.64 \times 10^{-1}(*)$	$4.55 \times 10^{-1}(*)$	$5.41 \times 10^{-1}(*)$	—
MC..ane → C..ane	$3.83 \times 10^{-2}(*)$	4.99×10^{-2}	2.60×10^{-16}	—
Phenol → C..one	—	—	—	—
Phenol → C..ol	—	—	—	—
Phenol → C..ane	—	—	—	—
C..one → C..ol	2.91×10^{-1}	$5.75 \times 10^{-1}(*)$	$8.37 \times 10^{-1}(*)$	2.04×10^{-1}
C..one → C..ane	3.34×10^{-2}	1.10×10^{-2}	1.13×10^{-12}	—
C..ol → C..ane	6.79×10^{-20}	1.70×10^{-5}	4.68×10^{-22}	—

Table S3: Effective model parameters by catalyst, with water as the solvent. Values under 1×10^{-6} are grayed out and assumed to be zero for pathway analysis. Values with asterisks $(*)$ were found to have a relatively lower impact on the model fit as identified by sensitivity analysis. Units are min^{-1}. (Key: C..ane=cyclohexane, C..ol=cyclohexanol, C..one=cyclohexanone, MC..ane=methoxycyclohexane, MC..one=methoxycyclohexanone)

Effective Rate Constant	Ru			Ni
	CAC	FWAC-meso	FWAC-micro	CAC
Guai → Placeholder	9.88×10^{-2}	$2.14 \times 10^{-1}(*)$	9.51×10^{-2}	1.93×10^{-2}
Placeholder → Guai	1.28×10^{-1}	2.27×10^{-2}	2.24×10^{-3}	2.96×10^{-2}
Guai → MC..one	6.87×10^{-3}	1.87×10^{-2}	7.83×10^{-3}	1.04×10^{-3}
Guai → MC..ane	—	—	—	—
Guai → Phenol	3.45×10^{-2}	1.05×10^{-1}	7.19×10^{-2}	1.45×10^{-3}
Guai → C..one	2.79×10^{-3}	3.92×10^{-3}	5.74×10^{-18}	4.65×10^{-5}
Guai → C..ol	2.58×10^{-5}	4.61×10^{-2}	7.93×10^{-3}	1.08×10^{-3}
Guai → C..ane	—	—	—	—
MC..one → MC..ane	—	—	—	—
MC..one → C..one	3.13×10^{-18}	1.98×10^{-22}	4.55×10^{-20}	1.72×10^{-16}
MC..one → C..ol	9.04×10^{-86}	$6.36 \times 10^{-3}(*)$	1.57×10^{-17}	3.34×10^{-2}
MC..one → C..ane	—	—	—	—
MC..ane → C..one	—	—	—	—
MC..ane → C..ol	—	—	—	—
MC..ane → C..ane	—	—	—	—
Phenol → C..one	$9.68 \times 10^{-2}(*)$	2.59×10^{-1}	$1.82 \times 10^{-1}(*)$	3.62×10^{-3}
Phenol → C..ol	1.63×10^{-1}	5.05×10^{-15}	1.73×10^{-16}	2.09×10^{-2}
Phenol → C..ane	—	—	—	—
C..one → C..ol	1.98×10^{-1}	$3.66 \times 10^{-1}(*)$	$3.98 \times 10^{-1}(*)$	6.57×10^{-5}
C..one → C..ane	—	—	—	—
C..ol → C..ane	—	—	—	—

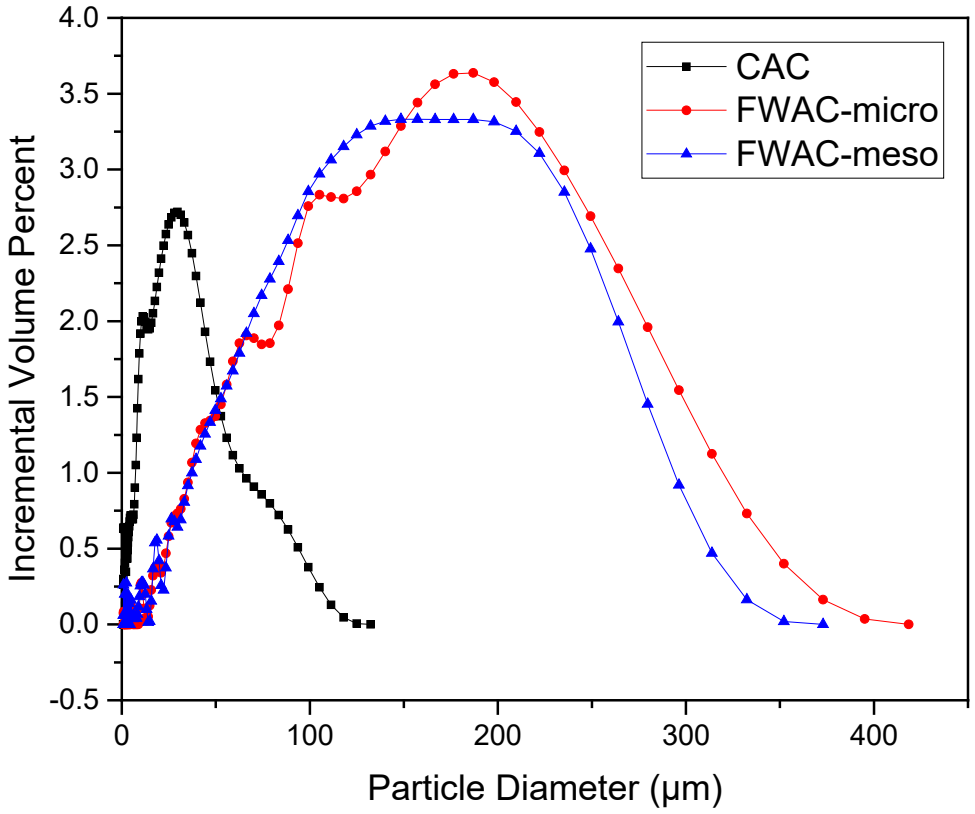

Figure S1: Distributions of particle diameters collected for each of the three AC supports. The CAC support shows a tighter and lower-average particle diameter distribution than either of the FWAC supports.

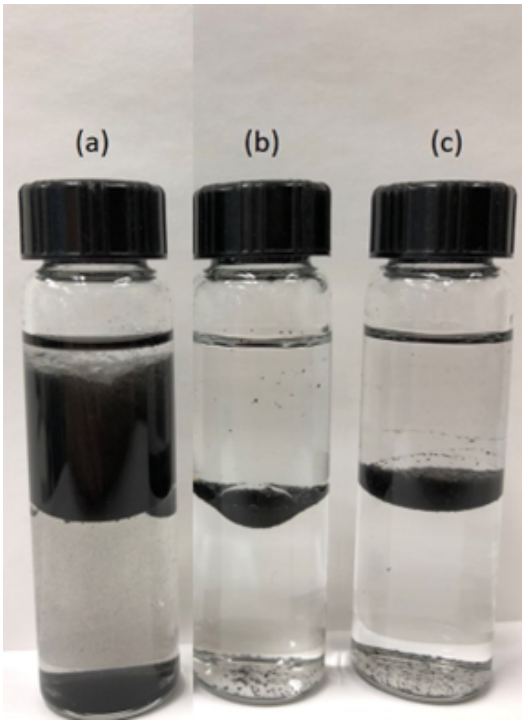

Figure S2: Results of the wettability test for the three AC supports. The ACs tested are: (a) CAC, (b) FWAC-micro, and (c) FWAC-meso. CAC particles were able to be suspended in the water phase (top), indicating a higher hydrophilicity than particles from either of the FWAC supports.

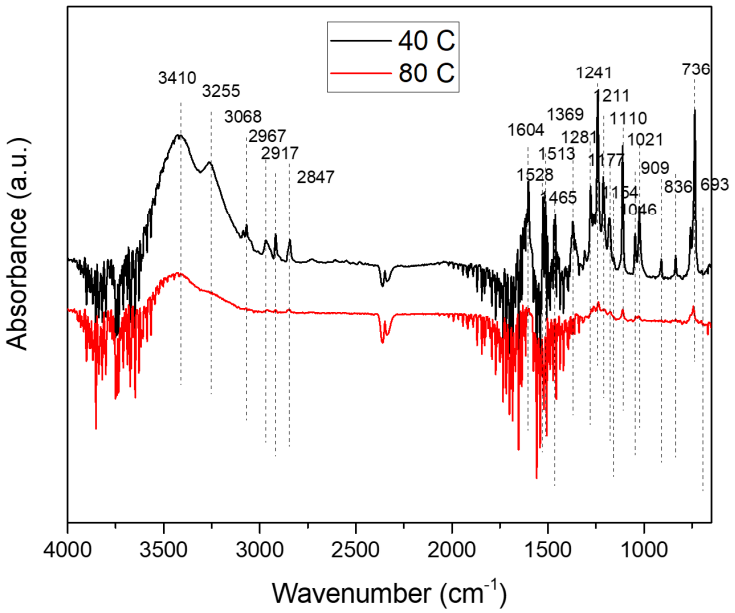

Figure S3: DRIFTS spectrum of pure guaiacol at 40 °C and 80 °C.

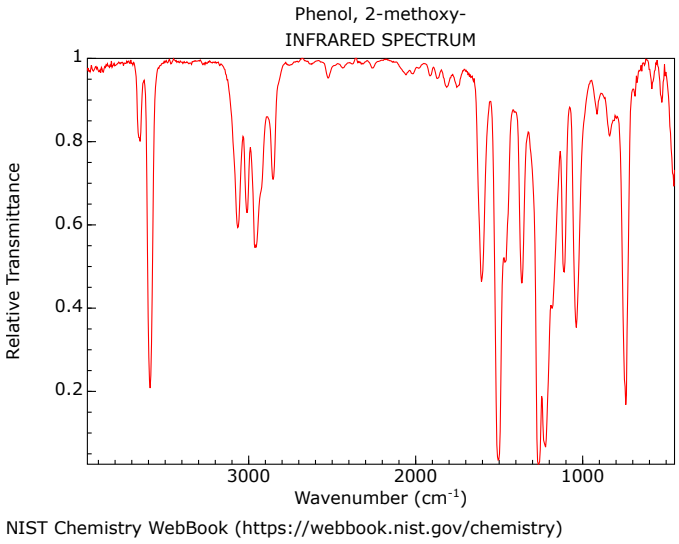

Figure S4: FTIR spectrum of guaiacol obtained from NIST.

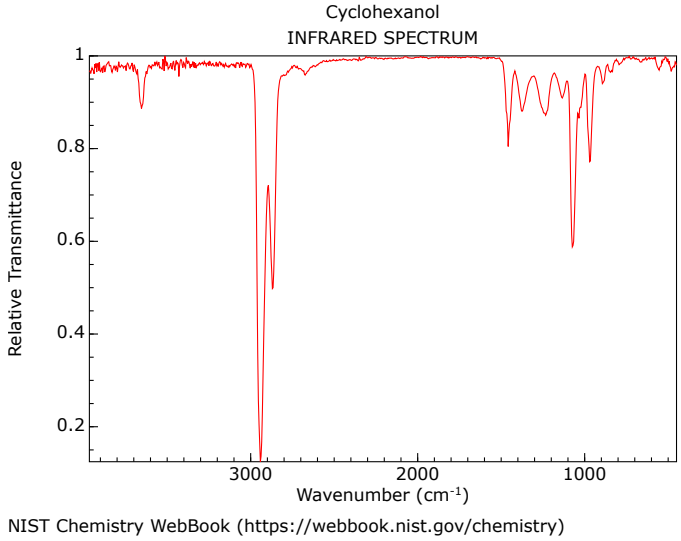

Figure S5: FTIR spectrum of cyclohexanol obtained from NIST.

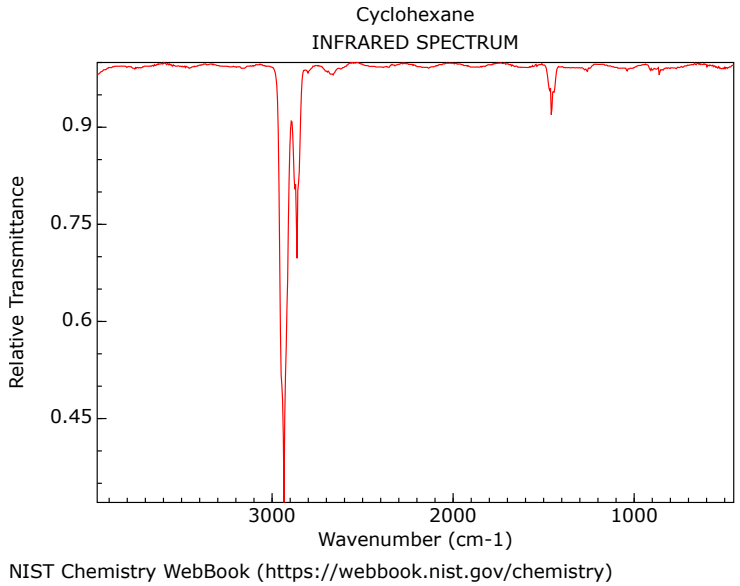

Figure S6: FTIR spectrum of cyclohexane obtained from NIST.